Hydrogen (or Syngas) Generation - Solar Thermal Chemical Energy Storage

Jonathan Scheffe, Dylan McCord, Diego Gordon
University of Florida
Department of Mechanical and Aerospace Engineering
Gainesville, FL 32611

Introduction

Solar energy is emitted from the sun in the form of electromagnetic radiation that closely approximates the spectral distribution of a blackbody at 5777 K, as described by Plank's Law[1]. Due to the inverse square law, the total solar irradiance decreases as the radiation travels from the sun to the earth's atmosphere, where it is approximately 1367 W m^{-2} (G_{on}*)[1]. As the solar radiation penetrates earth's atmosphere, it is attenuated through light scattering and absorption, further decreasing the total irradiance (G_n†)[1]. The resultant solar spectral irradiance for air mass ratios (m)‡ of 1 and 1.5, as well as extraterrestrial and that of a blackbody at 5777 K are shown in Figure 1[2]. As seen for m = 1 (orange) and 1.5 (gray) solar irradiance decreases for small wavelengths due to scattering and at higher wavelengths in selected bands due to absorption, primarily by H_2O, CO_2 and O_3. The resultant total irradiation for m = 1 and 1.5 is 934 and 814.9 W m^{-2}, respectively. As seen, the majority (48%) of the solar radiation falls in the visible range (380 nm < λ < 780 nm), followed by 46 % in the infrared (λ > 780 nm) and 6% in the ultraviolet (λ < 380 nm). The sun's energy may be considered as discrete packets of quantized energy, or photons, whose energy (E_{photon}) is dependent on its wavelength (λ), or frequency (ν), as described mathematically by:

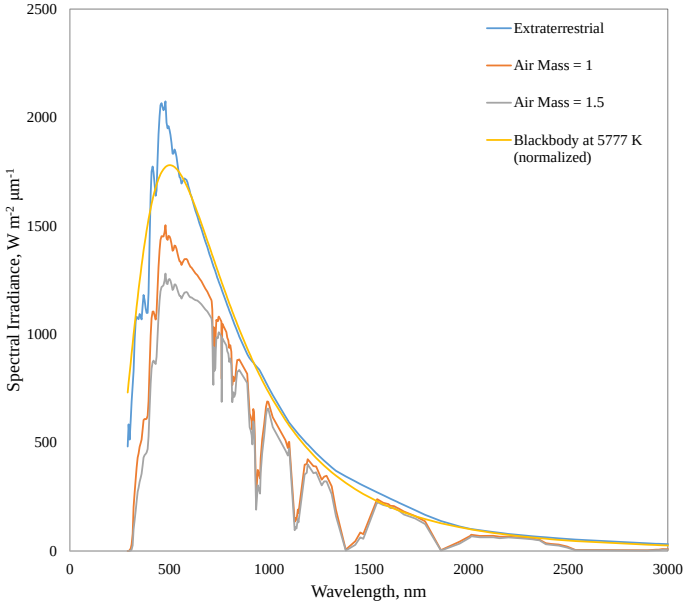

Figure 1. Solar spectral irradiance versus wavelength for extraterrestrial radiation, m = 1 and m = 1.5. For reference the normalized spectral distribution of a blackbody at 5777 K is included. For air mass calculations, α = 0.66 and β = 0.085.

$$E_{photon} = h\nu = hc/\lambda \quad (1.1)$$

where h is planks constant (6.6256 x 10^{-34} J s or 4.1357 x 10^{-15} eV s) and c is the speed of light specific to the medium through which it is traveling.

Because of earth's rotation on its axis and the varying declination of the sun with respect to earth's equator, the spectral irradiance varies with time of day and year for a fixed position on earths surface[1]. Therefore, as solar energy conversion technologies become cheaper (such as photovoltaics), there is a growing demand to store this energy in a form where it can be used on demand rather than relying on traditional fossil technologies when the sun isn't shining. The conversion of solar energy into chemical means (i.e. hydrogen or syngas§), hereby referred to as solar fuels, is one pathway among several (e.g. thermal, batteries**, pumped hydro, compressed air, etc.) that has the potential to be cost effective and efficient, while and at the same time capable of converting solar energy into transportable fuels such as hydrogen, gasoline, diesel and kerosene, several of which are compatible with our energy infrastructure as it stands today.

---

* G_{on} is the irradiance on a surface normal to propagation outside earth's atmosphere

† G_n irradiance on a surface normal to propagation inside earth's atmosphere

‡ m is a ratio of the atmosphere mass through which radiation passes to that of the atmosphere mass through which it passes when the sun is at its zenith

§ Synthesis gas is a mixture of H_2 and CO, usually with a H_2/CO ratio from 1/1 to 3/1

** While batteries do constitute a form of chemical energy storage, they are more formally an electrochemical energy storage pathway and will not be discussed in this chapter

Storage of Solar Energy in Chemical Bonds

Motivating chemical energy storage is the fact that compared to batteries, the gravimetric energy density of fuels such as diesel are 100 times greater[3]. Further, fuels such as diesel, gasoline and kerosene are readily integrated with our current energy infrastructure and offer the possibility of long term, seasonal storage. The conversion of solar energy into fuels may involve either the direct (photons or thermal energy) or indirect (electrons from an alternative storage technology or stored thermal[*]) utilization of solar energy to drive an endothermic chemical reaction while the sun is plentiful. This can be described easily using the example of water dissociation into H_2 and O_2, as shown below.

$$H_2O\ (l) \leftrightarrow H_2\ (g) + 0.5O_2\ (g)\ (\Delta h = 285.8\ kJ\ mol^{-1})\ (1.2)$$

In the forward direction the reaction is not spontaneous and requires energy to proceed. This energy is equal to the enthalpy of reaction (Δh) and for water dissociation is 285.8 kJ per mol H_2O or 2.962 eV at 298.15 K[4]. When reversing the reaction, the reaction enthalpy may be released to provide heat and drive a thermodynamic cycle such as a fuel cell[5] or heat engine[6].

The conversion of sunlight to fuels (H_2 itself being one) may be accomplished through a variety of pathways as indicated in Figure 2, some of which even occur in nature such as photosynthesis[†]. In all scenarios, the primary energy source is photons from the sun and the primary feedstocks to be considered here are H_2O and/or CO_2. Only these feedstocks are considered as they are the primary byproducts of high energy density liquid fuel or H_2 combustion and constitute a convenient form of energy storage that has the potential to operate in a closed loop cycle (i.e. no net emissions) if coupled with sequestration.

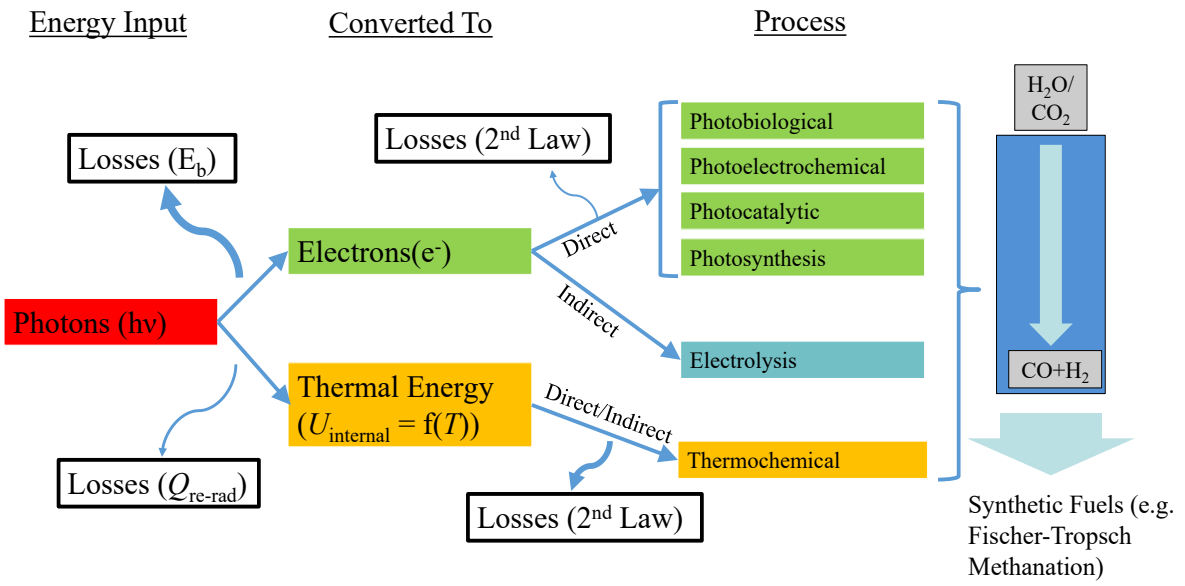

Figure 2. Potential pathways to convert solar energy to combustible fuels. The two primary pathways involve conversion of photons to free electrons or their absorption as thermal energy. The processes shown here are not exhaustive.

[*] This is similar to the working principle of concentrated solar power plants coupled with thermal storage. There, a working fluid such as molten salt is heated during the day and stored in a thermal reservoir. The thermal energy from the reservoir is then extracted on demand to run a power plant 24/7.[1]

[†] Photosynthesis is essentially the conversion on photons, water and carbon dioxide to carbohydrates. The reversible reaction, which releases energy can easily be seen by burning plant matter which produces heat.

Photons ("Energy Input", far left side of Figure 2) may be used to drive the process of interest either through its conversion to a free electron or through absorption and the generation of heat ("Converted To", middle of Figure 2). These energy forms may then be used to drive the endothermic reduction of H_2O and/or CO_2 via a variety of processes ("Processes", right side of Figure 2) to produce either H_2 and or synthesis gas ($CO + H_2$), the building blocks of synthetic fuels[*]. For many catalytic pathways that convert H_2O and or CO_2 to fuels this is a simplified explanation; rather than produce synthesis gas the hydrocarbon fuel is directly converted[7]. For example, consider the photo-assisted catalytic conversion of H_2O and CO_2 into methane or other hydrocarbon fuels.[8]

Electron Driven Processes

The conversion of photons to free electrons may be achieved in a semiconductor by ejecting an electron from the semiconductor's valence band to the conduction band; this occurs if the photon energy is greater than the semiconductor's bandgap energy (E_G). For example, E_G of Silicon (Si), a ubiquitous semiconductor used in the solar industry, is 1.1242 eV[9], meaning that photons with wavelengths equal to or less than 1.104 μm can eject electrons to the conduction band with exactly this energy; photons with larger wavelengths are either absorbed as heat, reflected or transmitted. The excess energy associated with smaller wavelength photons is also primarily released as heat[†]. The ejected electrons may then be used to drive a variety of processes, either directly or indirectly, such as those highlighted in Figure 2. Direct usage is referred to applications in which electrons are ejected and utilized within the same process, such as photoelectrochemical production of H_2[10], where the semiconductor and electrode exist as a single photoelectrode. Indirect is referred to as the coupling of two independently operating processes, such as photovoltaic energy production to generate electrical energy, followed by electrolysis of water.

Thermally Driven Processes

Photons may also be absorbed thermally in a medium to generate heat, which may then be used for a variety of applications (a straightforward and ubiquitous usage is solar driven hot water heaters). However, in this chapter we are concerned with applications in which the heat is used to drive chemical reactions; hereby referred to as thermochemical reactions. Thermochemical reactions may refer to simple reversible chemical reactions in which the reaction is driven in the forward direction when energy is available reversed to release heat on demand (e.g. Co_3O_4 (s) ↔ 3CoO (s) + $0.5O_2$ (g))[11], or reactions in which the solar derived heat is converted to combustible fuels such as H_2 or synthesis gas. The conversion to fuels is typically a more energetic process than the former and requires higher temperatures (usually between 1000 and 2000 K) because the nature of gases from which they are derived; namely H_2O or CO_2 which are inherently extremely stable molecules. Because the entire solar spectrum is capable of being utilized if photons are absorbed as heat[‡], and the reactions operate at elevated temperatures, these processes offer a thermodynamically attractive pathway to solar fuel production[12]. A more detailed discussion follows in the section below entitled "Solar Thermochemical Processes".

Solar Concentration and Absorption as Heat

In order to achieve temperatures suitable to drive thermochemical reactions, sunlight is usually concentrated[§], through a variety of possible mechanisms, to increase the radiative flux on an absorbing surface. Usually 3-D point focused concentration (as opposed to lower concentration line focus 2-D

[*] Synthesis gas is the basic building block to a range of synthetically derived fuels (e.g. diesel, kerosene, etc.) via catalytic pathways such as Fischer-Tropsch synthesis or methanation.

[†] For most processes that utilize electrons, the production of heat is usually not desirable.

[‡] Either using materials that have high absorptivity over the entire solar spectrum, such as Pt black, or through the design of a blackbody enclosure which ensures that there are enough internal reflections that incident photons are eventually absorbed

[§] Concentration (C) refers to the use of reflecting or refracting optics to concentrate sunlight beyond the typical value of 1 kW m^{-2}, or 1 sun, to values as high as 10000 kW m^{-2}, or 10000 suns.

technologies), such as a parabolic dish, heliostat field or Fresnel concentrator, is required to achieve the concentration ratios necessary (>1000 suns)[1, 13, 14] for driving these high temperature processes. An exemplary demonstration of 3-D optical concentration shown in 2-D is shown below in Figure 3 using a parabolic shape. Here, incident photons with irradiance G over and area A_1, are reflected to a focal plane with irradiance G_{in} and area A_2. The reflected photons are not reflected to a single point because of imperfections in the mirror surface and a non-zero solid angle formed between the earth and sun (i.e. sun rays are not perfectly parallel). Assuming perfect reflectivity and no spillage (radiation that does not fall within the aperture), then the total power ($\dot{Q}_{in}$) at each plane (shown in dashed and solid vertical lines) should be equivalent according to the first law of thermodynamics, and thus $GA_1 = G_{in}A_2$. The ratio of G_{in}/G, or A_1/A_2 in the case of perfect reflectivity, is referred to as the optical concentration ratio (C) and is a measure of the increase in radiative flux as a result of concentration. Any reflectivity less than unity or

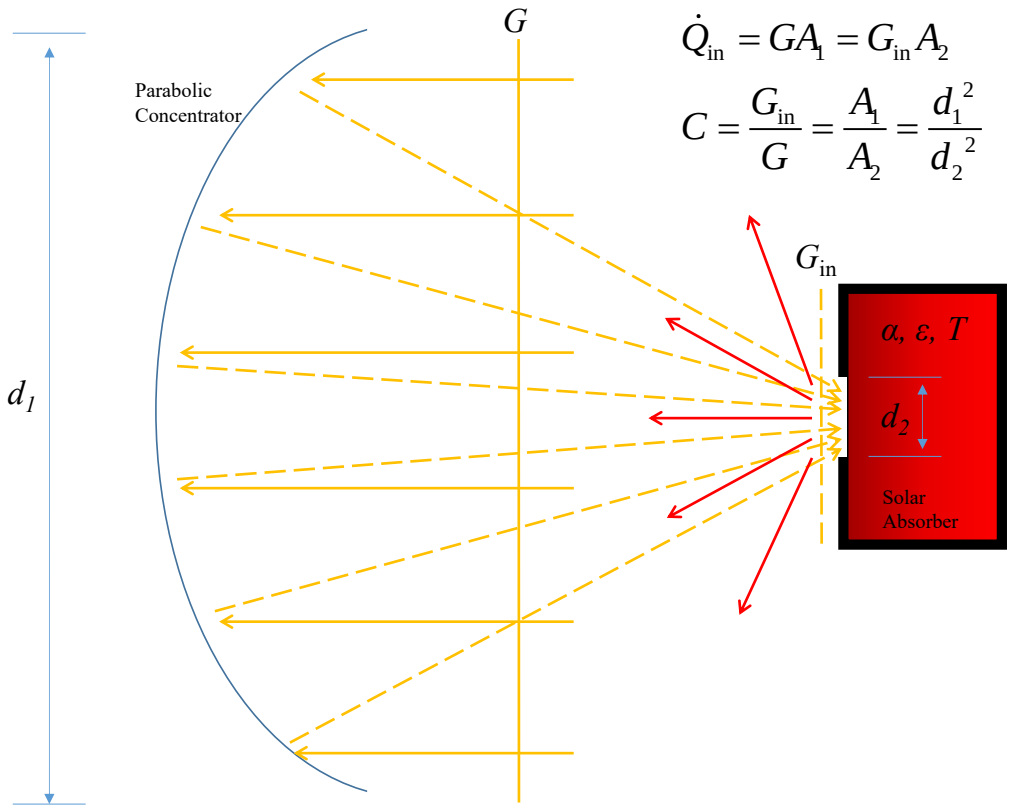

Figure 3. Schematic depicticing solar concentration in three dimensions using a 2-D parabolic shape. Radiation (solid yellow lines) is incident normal to the projected area of the parabolic surface, where it is reflected towards its focal point (yellow dashed lines). The concentrated radiation is then absorbed in a solar absorber which re-radiates to its surroundings at a rate proportional to its temperature to the fourth power.

spillage losses will cause the optical concentration to decrease in a proportional manner. Refer to Steinfeld and Palumbo[15] for a general discussion and for a more detailed discussion refer to a textbook on geometric optics[16, 17].

Following concentration and entrance through the aperture, the thermal radiation is absorbed in a cavity or receiver as heat, some of which then re-radiates back to the surroundings (shown in red). This re-radiation is referred to as radiative losses ($\dot{Q}_{rad}$) that inherently occur as temperature increases. Overall, $\dot{Q}_{rad}$ is proportional to the emissivity (ε) of the absorbing cavity (for a blackbody $\varepsilon = 1$), the Stephan-Boltzmann constant ($\sigma = 5.67 \times 10^{-8}$ W m^{-2} K^{-4}), the aperture area through which radiation passes, in this case A_2, and its temperature to the fourth power, shown mathematically below.

$$\dot{Q}_{rad} = \varepsilon\sigma A\left(T^4 - T_{surroundings}{}^4\right) \approx \varepsilon\sigma A T^4 \quad (1.3)$$

The absorption efficiency (η_{abs}) of solar irradiance to heat is defined as the amount of radiation absorbed ($\dot{Q}_{abs}$) divided by $\dot{Q}_{in}$. Thus, mathematically η_{abs} decreases with temperature to the fourth power and increases with increasing concentration ratio, as shown below.

$$\eta_{abs} = \frac{\dot{Q}_{abs}}{\dot{Q}_{in}} = \frac{\dot{Q}_{in} - \dot{Q}_{rad}}{\dot{Q}_{in}} = 1 - \frac{\varepsilon\sigma T^4}{GC} \quad (1.4)$$

It is typical for solar cavity receivers to approach absorptivity's of a blackbody ($\alpha = \varepsilon \approx 1$) because of the large number of internal reflections. η_{abs} versus temperature plotted for concentration ratios from 1000 to 10000 suns are shown in Figure 4. They can be seen in the top solid curves that begin at 1 and decrease to zero at elevated temperatures. As seen, η_{abs} increases with increasing concentration ratio for a fixed temperature because the area through which re-radiation may occur is decreased (aperture area has to decrease in order for C to increase).

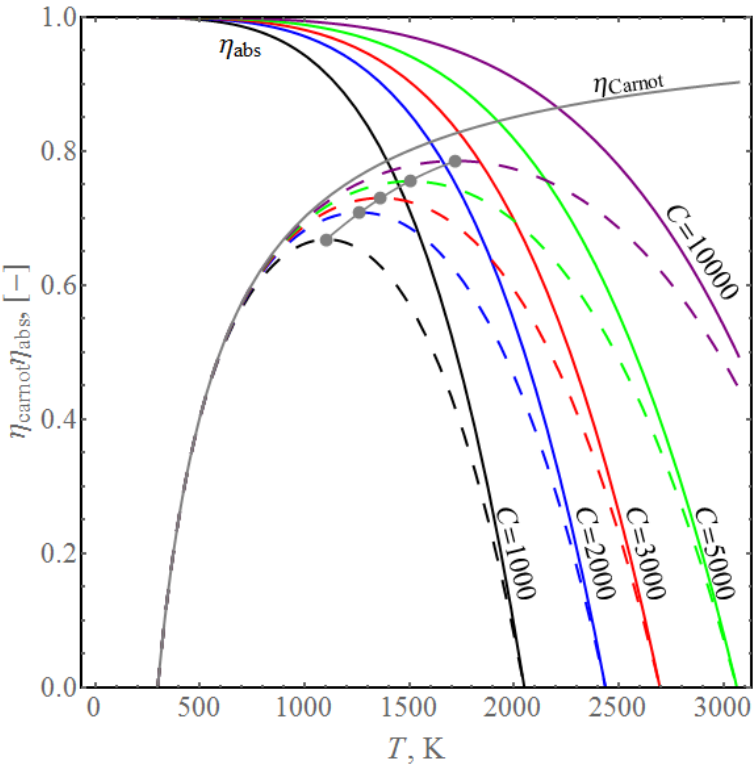

Figure 4. Dashed lines represent the maximum theoretical solar to fuel efficiency via thermochemical pathways. These lines are the product of the absorption efficiency, which decreases with temperature to the fourth power, and Carnot efficieny which increases with increasing operating temperature. Insprired by Fletcher and Moen, Science, 1977.[16]

Ultimately, it is the aim of solar thermochemical fuel processes to convert the net heat that is absorbed, to work (in this case the work is considered to be H_2 or synthesis gas). In a seminal Science publication in 1977 by Fletcher and Moen[18], this is shown to be limited by the product of the Carnot efficiency (η_{Carnot}) and η_{abs}, where η_{Carnot} is defined as:

$$\eta_{Carnot} = 1 - \frac{T_{low}}{T} \quad (1.5)$$

Here the low temperature (T_{low}) is the temperature at which the fuel is eventually combusted and the high temperature (T) is the temperature at which solar energy is used to drive the chemical reaction of interest (e.g. $H_2O \rightarrow H_2 + 0.5O_2$). The product of η_{abs} and η_{Carnot} is therefore the maximum efficiency (η_{max}) at which one could convert solar energy to fuels[18]. η_{abs}, η_{Carnot} and $\eta_{Carnot}\eta_{abs}$ are all plotted in Figure 4 and as expected, there is a peak efficiency for a given concentration ratio where the efficiency is maximized (gray points). In general the temperature where peak efficiency occurs increases with increasing concentration ratio. Importantly, this shows that for

realistically high concentration ratios* (e.g. 500-5000 suns), maximum solar to fuel conversion efficiencies are greater than 70%. In terms of the economics of solar fuel processes, the efficiency is the principle metric that dictates the economic viability, or levelized cost of energy (LCOE), of the process because it directly scales with the amount of capital equipment required[14].

Solar Thermochemical Processes

There are several approaches to convert absorbed solar energy to fuels via thermally driven, or "thermochemical" pathways. The primary pathways through which solar thermochemical conversion to H_2

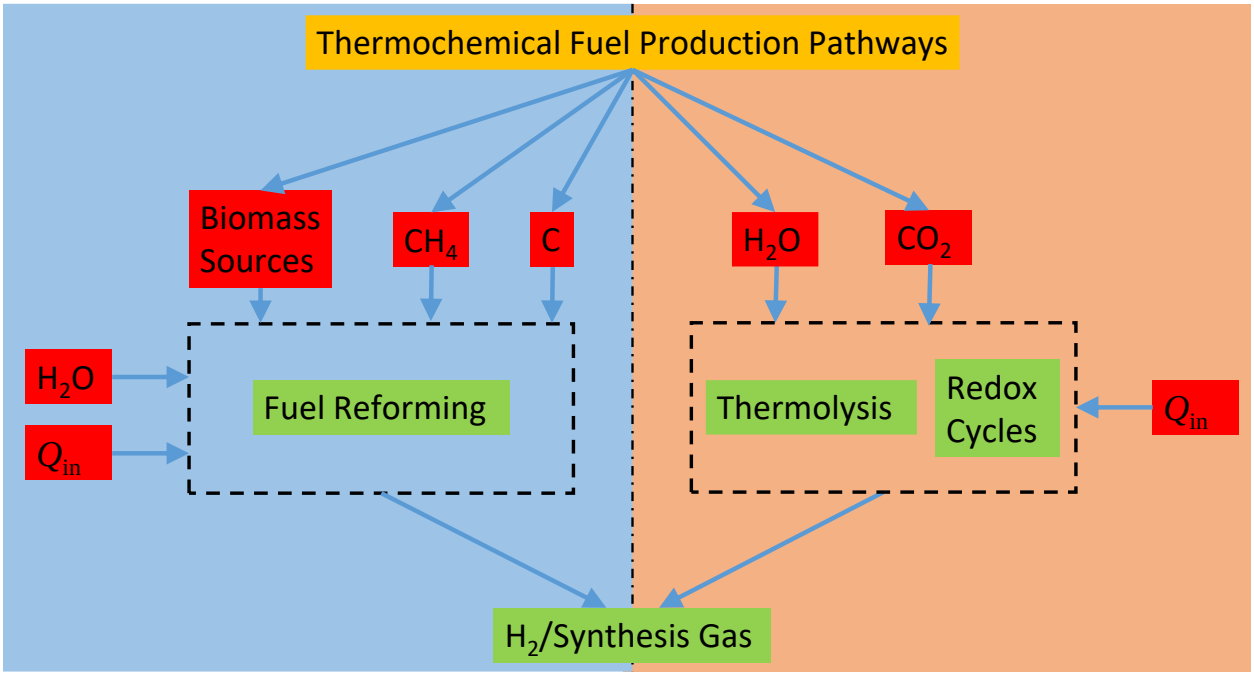

Figure 5. Thermochemical fuel production pathways that utilze concentrated sunlight to drive an endothermic resulting in H_2 or synthesis gas. On the left are fuel reforming cycles drive an endothermic reforming reaction and on the right are pathways that only utilize H_2O or CO_2 as net feedstocks.

or synthesis gas can be achieved are either fuel reforming processes (e.g. steam methane reforming) where a fuel and H_2O (and sometimes CO_2) are used as feedstocks, or thermolysis/redox cycles in which no fuel precursor is required and only H_2O or CO_2 are used as feedstocks. These are both indicated on the left and right hand sides in Figure 5, respectively. A detailed description of these processes, especially with respect to their thermodynamics, will be the remaining focus of this chapter.

Solar Reforming Processes

For most fuel reforming process that are non-solar, some of the carbonaceous feedstock is combusted (e.g. CH_4 (g) + $2O_2$ (g) → $2H_2O$ (g) + CO_2 (g)) to provide the heat necessary heat to drive an endothermic reforming reaction (CH_4 (g) + H_2O (g) → $3H_2$ (g) + CO (g)). As a result, the net heating value of the products is less than the primary feedstock. For example, consider steam methane reforming which is the most established method to produce industrial H_2. Here, the net steam reforming reaction may be expressed by:

H_2O (l) + CH_4 (g) → $3H_2$ (g) + CO (g) (1.6)

* Realistically in the sense that when the concentration ratio approaches extreme values (e.g. 10000 suns) the spillage is usually so high because of imperfect optics that it is not practical for most applications.

This reaction is the net reaction of the following three formation reactions

H_2O (l) → H_2 (g) + 0.5O_2 (g), -$\Delta H°_{f,H2O}$ = 285.83 kJ @ 298.15 K (1.7)

CH_4 (g) → C (s) + 2H_2 (g), -$\Delta H°_{f,CH4}$ = 74.873 kJ @ 298.15 K (1.8)

0.5O_2 (g) + C (s) → CO (g), $\Delta H°_{f,CO}$ = -110.527 kJ @ 298.15 K (1.9)

where $\Delta H°_{f,i}$ is the standard formation enthalpy of species i at standard conditions (298.15 K). Thus, the net reaction enthalpy of the steam reforming reaction (-$\Delta H°_{f,H2O}$ + -$\Delta H°_{f,CH4}$ + $\Delta H°_{f,CO}$) is 250.2 kJ at 298.15 K. To drive this endothermic reaction, some of the methane feedstock is combusted according to the following reaction:

2O_2 (g) + CH_4 (g) → 2H_2O (l) + CO_2 (g) (1.10)

which is a product of the following formation reactions.

CH_4 (g) → C (s) + 2H_2 (g), -$\Delta H°_{f,CH4}$ = 74.873 kJ @ 298.15 K (1.11)

O_2 (g) + C (s) → CO_2 (g), $\Delta H°_{f,CO2}$ = -393.522 kJ @ 298.15 K (1.12)

O_2 (g) + 2H_2 (s) → 2H_2O (l), 2$\Delta H°_{f,H2O}$ = -571.66 kJ @ 298.15 K (1.13)

Thus, the net reaction enthalpy (-$\Delta H°_{f,CH4}$ + $\Delta H°_{f,CO2}$ + 2$\Delta H°_{f,H2O}$) is -890.3 kJ at 298.15 K. Therefore, for every mole of CH_4 that is reformed (1.6) that requires 250.2 kJ, 0.28 moles must be combusted (1.10) to provide the require process heat, at a minimum (250.2 kJ/890.3 kJ = 0.28). In reality it is substantially greater because of inefficiencies and because the reaction enthalpy decreases at higher temperatures (e.g. for methane combustion $\Delta H°$ = -800 kJ at 900 K)[4]. For a more thorough description of reaction enthalpies and their temperature dependence refer to Introduction to Chemical Engineering Thermodynamics 7th Edition, specifically Chapter 4 entitled Heat Effects[19], or another appropriate thermodynamics or chemistry textbook.

In solar-driven fuel reforming processes, solar energy is used as process heat to drive the endothermic reforming reaction rather than combustion of the feedstock[20]. As a result the feedstock is "upgraded"

Figure 6. On the left is the STARS solar methane reforming reactor with the aperture for sunlight on its right hand side. On the left is the STARS systems mounted to a tracking parabolic concentrator for prototype testing.[28]

because the heating value of the products are greater than the primary feedstock, and solar energy is effectively stored in chemical form. A wide variety of solar reforming processes have been proposed in the literature, and compared to the non-fuel reforming processes on the right side of Figure 5, these typically occur at relatively moderate temperatures (e.g. < 1000 °C). Therefore, they are practically more straightforward because demands on reactor and construction materials are not as strict. As a result, these technologies are relatively mature and several concepts have been tested at the prototype reactor scale. For example, reactors have been developed and tested for the reforming of natural gas[21], methanol[22], activated carbon[23], coal[23], coke[23, 24], beech char[25], biochar[26], bagasse[27], corn stover, Kentucky bluegrass[28], and a wide variety of industrial waste products[29]. It is important to note that solar reforming processes are not carbon neutral unless the carbon comes from a source that is continuously replenished by CO_2 from the atmosphere (e.g. algae, corn stover, bagasse, etc.).

To date, the highest reported efficiency for solar driven steam methane reforming is 69% by Wegnag et al. from Pacific Northwest National Laboratory (PNNL)[30]. Here, the efficiency is defined as the change in the heating value between the products (syngas) and reactants (methane) divided by the solar power input. A photograph of their reactor, which they call solar thermochemical advanced reactor system (STARS) can be seen in Figure 6 on the left. The concept combines an aperture where concentrated sunlight enters that is coupled with a catalytic methane reforming system based on micro and meso channel reactors and heat exchangers. The micro and meso channel heat exchanger/reactor system was developed independently of any intended solar applications over several decades and recently adopted to meet the demands of concentrated solar applications. An example of the system mounted to a parabolic dish is shown in Figure 6 on the right. The upper operating temperature is on the order of 840 °C, moderate by gas splitting solar thermochemical standards, and this technology nicely demonstrates the potential maturity, robustness and feasibility of solar driven reforming while operating under realistic conditions. Current barriers to commercialization likely lie in the overall cost of the reactor system, integration with syngas storage because of the inherently transient nature of the sun and startup/shutdown associated with nighttime and cloud cover. These are issues that all concentrated solar syngas systems must consider.

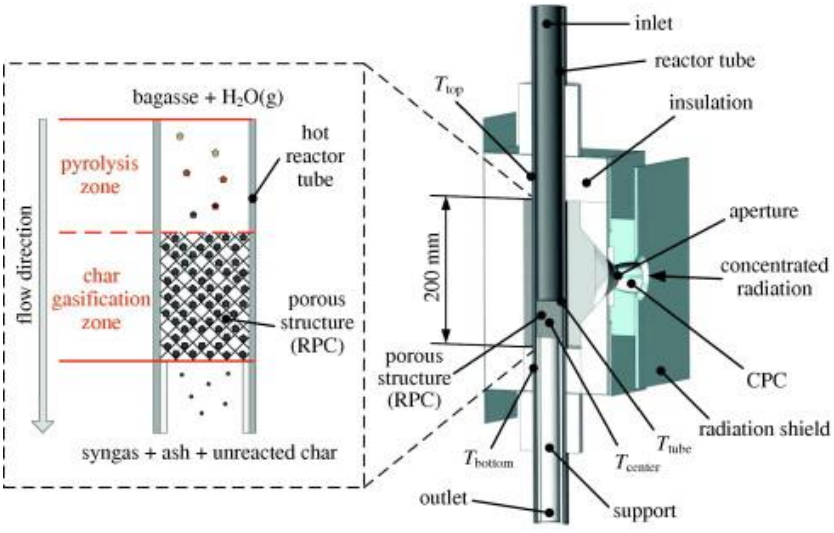

Figure 7. From Steinfeld *et al*. Solar driven bagasse reactor to produce synthesis gas.[25]

An example of a prototype aerosol reactor, developed by Steinfeld *et al*. and used for the reformation of bagasse (sugar cane residue) particles[27] is shown in Figure 7. Here, solid bagasse particles and H_2O (g) enter a tubular reactor that is housed within an insulated cavity type solar receiver. Concentrated radiation enters through the receiver aperture (right side), is further concentrated in a secondary concentrator (here a compound parabolic concentrator, or CPC[*]). Initially the bagasse is rapidly pyrolyzed in the pyrolysis zone, where the bagasse is converted to char and

[*] CPC is short for Compound Parabolic Concentrator, a nonimaging concentrating device that increases the geometric concentration ratio (A_{in}/A_{out}). Refer to Winston's text entitled *Nonimaging Optics*. ([16] R. Winston, J. C. Miñano, P. G. Benitez, Nonimaging optics, Academic Press, **2005**.)

undesired secondary products such as ash. Following pyrolysis it is gasified, or reacted with H_2O (g), to form synthesis gas. Because the gasification reaction occurs relatively slowly, this aerosol reactor incorporated a porous structure to increase the residence time of the char particles in the hot zone. Depending on the reactant composition and structure, a variety of reactor configurations have been proposed, but their discussion is outside of the scope of this chapter. Please refer to the following citations for a more detailed description of several concepts; refs[20-29].

Solar Driven Thermolysis

Conceptually, the simplest path to H_2 or synthesis gas is the direct thermolysis of H_2O or CO_2. Additionally, these pathways are inherently carbon neutral, as opposed to fuel reforming processes, because their net inputs are simply the byproducts of fuel combustion. Their net chemical reactions are shown below.

$$H_2O\ (l) \rightarrow H_2\ (g) + 0.5O_2\ (g),\ -\Delta H°_{f,H2O} = 285.83\ kJ\ @\ 298.15\ K^4 \quad (1.14)$$

$$CO_2\ (g) \rightarrow CO\ (g) + 0.5O_2\ (g),\ \Delta H°_{CO2} = 283.0\ kJ\ @\ 298.15\ K^4 \quad (1.15)$$

Where $\Delta H°_{CO2}$ is the enthalpy change of CO_2 thermolysis referenced to standard state. This reaction enthalpy change is determined by recognizing that it is the sum of the following two formation reactions ($\Delta H°_{CO2} = -\Delta H°_{f,CO2} + \Delta H°_{f,CO}$) shown below.

$$CO_2\ (g) \rightarrow C\ (g) + O_2\ (g),\ -\Delta H°_{f,CO2} = 393.522\ kJ\ @\ 298.15\ K \quad (1.16)$$

$$C\ (g) + 0.5O_2\ (g) \rightarrow CO\ (g),\ \Delta H°_{f,CO} = -110.527\ kJ\ @\ 298.15\ K \quad (1.17)$$

While conceptually simple, these reactions are difficult to achieve in practice because of their extreme temperatures (usually $\geq$ 2273 K) and the favorability of the reverse reactions as the gaseous products cool. Thus, to prevent product recombination, thermolysis reactions are usually conducted in a high temperature oxygen conducting ceramic, such as ZrO_2, where the outside of the ceramic is kept at a low oxygen partial pressure[31, 32]. As the reaction progresses, the produced O_2 diffuses across the solid membrane and away from either H_2/CO, thereby preventing recombination. Other techniques such as rapid quenching of the product gases have been utilized but with limited success[31]. Usually thermolysis reaction temperatures are limited by the temperature stability of the oxygen conducting ceramic (usually less than 2273 K) or other reactor construction materials and are therefore conducted well below where they are thermodynamically favorable at ambient pressure ($\Delta G_{rxn} >> 0$ at 2273 K). As a result, reaction extents are usually very small or a large amount of mechanical work (e.g. vacuum pumping) is required. In both instances, the efficiency is hindered; in the former, an excess of thermal energy is supplied that may only be recovered through efficient, high temperature heat exchange, or the latter because of the second law losses associated with producing the work. Further, even if materials were stable enough to operate where the reactions are more thermodynamically favorable, the re-radiation losses would be so large that they would have a severe and negative effect on the efficiency (c.f. Figure 4).

Thermochemical Redox Cycles - Background

Rather than using electrical work, another possibility to decrease the operating temperature of H_2O or CO_2 thermolysis while still utilizing only thermal energy is through the implementation of a redox cycle where the thermolysis reaction is split into two or more reactions, where one of them has a larger entropy change than the net entropy change of the reaction[33, 34]. In general, as the number of reactions increases, the upper operating temperature decreases but the complexity associated with the process increases[33]. Therefore for

practical reasons, the bulk of interest in H_2O/CO_2 redox splitting cycles in recent years has been focused on two-step cycles.

Most two-step redox cycles drive a high temperature endothermic reduction of a solid metal oxide (MeO) in the first step (solar driven step); temperatures are typically greater than 1000 °C and dependent on the metal oxide used*. Following reduction, the reduced metal oxide (Me) is then subsequently oxidized in an exothermic reaction at lower temperatures by H_2O or CO_2 to re-oxidize it produce gaseous H_2 or CO. The net reaction is simply the dissociation of H_2O or CO_2[35]. The two step MeO based redox cycle for H_2O splitting and the net reaction is shown below.

$$\mathrm{MeO} \xrightarrow{\Delta H_{red}} \mathrm{Me} + 1/2\,\mathrm{O_2(g)} \quad \text{Reduction Step 1)} \quad (1.18)$$

$$\mathrm{Me} + \mathrm{H_2O(g)} \xrightarrow{\Delta H_{ox}} \mathrm{MeO} + \mathrm{H_2(g)} \quad \text{Oxidation Step 2)} \quad (1.19)$$

$$\mathrm{H_2O(g)} \xrightarrow{\Delta H_{H2O}} \mathrm{H_2(g)} + 1/2\,\mathrm{O_2(g)} \quad \text{Net Reaction)} \quad (1.20)$$

The reason that these cycles result in a lower operating temperature than the direct thermolysis of H_2O (or CO_2) is that the first step takes advantage of the fact that the entropy change (ΔS) required to reduce the oxide is greater than for water dissociation (but also enthalpy is greater). For example, refer to the left subplot of Figure 8 that shows the Gibbs free energy change (ΔG) for the reduction reaction of a hypothetical metal oxide in blue alongside the H_2O thermolysis reaction in black. The equilibrium of both reactions is dictated by ΔG, where less than 0 indicates the reaction is more favorable in forward direction and greater than zero more favorable in the reverse direction. $\Delta G = \Delta H - T\Delta S$, and as seen here the entropy change is greater (steeper slope) for the oxide reduction, resulting in $\Delta G = 0$ at a lower temperature, meaning the reaction is more likely to proceed in the forward direction compared to thermolysis.

The oxidation of the reduced oxide with H_2O is the sum of the following two reactions.

$$\mathrm{Me} + 1/2\mathrm{O_2(g)} \rightarrow \mathrm{MeO} \quad (1.21)$$

$$\mathrm{H_2O(g)} \rightarrow \mathrm{H_2(g)} + 1/2\mathrm{O_2(g)} \quad (1.22)$$

$$\mathrm{Me} + \mathrm{H_2O(g)} \rightarrow \mathrm{MeO} + \mathrm{H_2(g)} \quad \text{Net Reaction)} \quad (1.23)$$

* Details of the metal oxides used will be discussed in subsequent sections.

The Gibbs free energy changes of reactions (1.21), (1.22) and (1.23) are shown on the right subplot of Figure 8. As seen, equations (1.21), (1.22) are simply the reverse of the oxide reduction and water thermolysis reactions and thus the oxide oxidation has a larger entropy change. The net reaction (1.23) (indicated in red) is simply the difference in ΔG between the two reactions. As seen, it is most negative at the lowest temperatures, indicating that oxidation is thermodynamically most favorable at the lowest temperature possible*. Effectively at these low temperatures the metal has a higher affinity for oxygen than H_2 does, as indicated by the more negative Gibbs at the lowest temperatures. However, as temperature increases, the reverse is true and oxidation becomes less favorable. Usually the oxidation temperature is conducted at the highest temperature possible where thermodynamics is not hindered because of improved

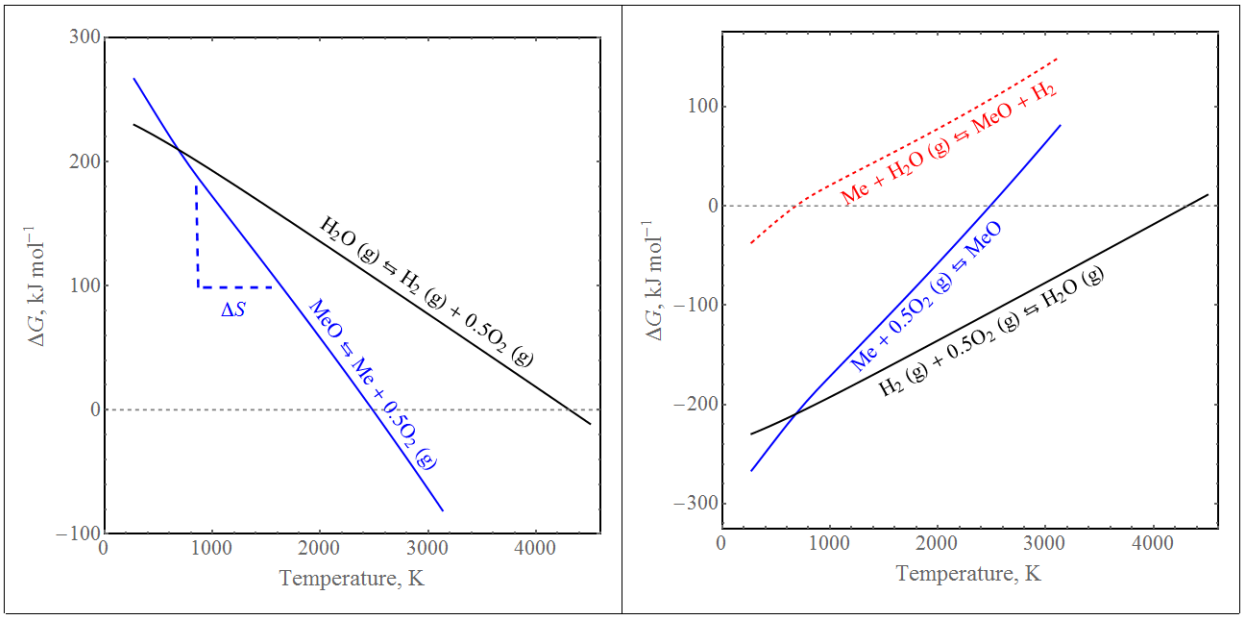

Figure 8. Left) Gibbs free energy change versus temperature of the water thermolysis reaction (black) and metal oxide reduction reaction (blue). Right) Gibbs free energy change versus temperature of the metal oxide oxidation reaction with steam (dashed red), oxygen (blue) and H_2 oxidation (black).

kinetics (i.e. more rapid reaction rates) and higher efficiencies because of smaller temperature swings between reduction and oxidation reactions that require a heat input. Descriptions of thermochemical redox cycles detailing this and the state of the art metal oxides used are reviewed in the ensuing sections (c.f. sections entitled Iron Oxide-based Redox Cycles, Ceria-based Redox Cycles, and Emerging Materials), but first the basics of reaction equilibrium will be discussed in order to better facilitate understanding.

Reaction Equilibrium

A basic understanding of the fundamental equations of chemical reaction equilibria and Gibbs free energy data may be used to appreciate the thermodynamic favorability of thermochemical reactions (or any chemical reaction). According to Smith and Van Ness[19], the general symbolic representation of a reversible chemical reaction may be expressed as:

$$aA + bB + \ldots \rightleftarrows cC + dD + \ldots \quad (1.24)$$

* It is important to note that the enthalpy change of the metal oxide reduction must be larger than the enthalpy change of water dissociation, or else there will be NO temperatures where the oxide oxidation is thermodynamically favorable.

Where A,B,C and D represent chemical formulas and a,b,c and d represent stoichiometric coefficients (ν). The equilibrium constant (K) of a reaction is defined as

$$K = \frac{a_C{}^c a_D{}^d \ldots}{a_A{}^a a_B{}^b \ldots} \quad (1.25)$$

Where a_i is the activity of species i. For an ideal gas where fugacity (f_i) is equal to the pressure (P) and the standard state pressure is 1 atm ($f_i° = P = 1$ atm), $a_i = x_i = p_i{}^*$. x_i is the molar fraction of species i and p_i refers to the partial pressure of species i. K is related to the standard Gibbs free energy change of a reaction ($\Delta G°$) according to:

$$\Delta G^\circ = -RT \ln K \quad (1.26)$$

where R is the ideal gas constant and T is temperature. Therefore, the equilibrium constant and standard Gibbs free energy change of reaction (1.14) assuming gas ideality at 1 atm total pressure is the following.

$$K_{H_2O} = \frac{p_{H_2} p_{O_2}{}^{1/2}}{p_{H_2O}} = \frac{x_{H_2} x_{O_2}{}^{1/2}}{x_{H_2O}} \quad (1.27)$$

$$\Delta G^\circ_{H_2O} = -RT \ln K_{H_2O} \quad (1.28)$$

Similar equations could be derived for reaction (1.15). When $\Delta G° > 0$ or $K < 1$, the reaction is more favorable in the reverse direction (e.g. denominator in (1.27) is greater than the numerator) and when $\Delta G° < 0$ or $K > 1$, the reaction is more favorable in the forward direction (e.g. numerator in (1.27) is greater than the denominator). Thus, K and $\Delta G°$ are an indicator of the thermodynamic favorability for the reaction to occur. It should be recognized that:

$\Delta G°_{H2O} = - \Delta G°_{f,H2O}$ and $K_{H2O} = 1/K_{f,H2O}$ (1.29)

and

$\Delta G°_{CO2} = -\Delta G°_{f,CO2} + \Delta G°_{f,CO}$ and $K_{CO2} = K_{f,CO}/K_{f,CO2}$ (1.30)

where $\Delta G°_{f,i}$ is the standard Gibbs free energy of formation of species i. $\Delta G°$ for H_2O and CO_2 thermolysis reactions (1.14) and (1.15) as a function of temperature, obtained from equilibrium data in NIST JANAF Thermochemical Tables[4], is shown in the left subplot of Figure 9. $\Delta G°$ is very large and does not equal 0 ($K = 1$) until 4310 K and 3339 K for H_2O and CO_2, respectively. These high temperatures make qualitative sense because these are known to be extremely stable molecules.

Equilibrium yields may be calculated in a straightforward manner with knowledge of either $\Delta G°$ or K. For this, the reaction coordinate (ε) is useful to utilize; ε effectively characterizes the extent to which a reaction has occurred. ε may be related to moles of species i at equilibrium (n_i) through the following relationship[19]:

$$\pm\varepsilon = \frac{\Delta n_i}{\nu_i} = \frac{n_i - n_{i,0}}{\nu_i} \quad (1.31)$$

* This comes from the fact that $a_i = f_i / f_i°$ and $f_i = x_i P = p_i$.

where $n_{i,0}$ is the initial number of moles present of species i and v_i is the stoichiometric coefficient of species i. A positive sign is attributed for product species and negative sign for reactant species. x_i is related to n_i and the total number of moles in the system, n_{total} by the following equation:

$$x_i = \frac{n_i}{n_{total}} = \frac{n_i}{\sum n_i} \quad (1.32)$$

Thus, the equilibrium constant (or $\Delta G°$) may be related to the reaction coordinate and the initial number of moles of each species in the system. If the equilibrium constant (or $\Delta G°$) is known as a function of temperature, then equilibrium yields of each species may then be determined, or vice versa. For example, consider a system in which 1 mole of H_2O (g) is initially present ($n_{H2O,0} = 1$) and knowledge of the final equilibrium yields of H_2O, H_2 and O_2 at a given temperature and pressure are desired. Combining(1.27), (1.31) and (1.32) the following two equations can be derived.

$$K_{H_2O} = \frac{x_{H_2} x_{O_2}^{1/2}}{x_{H_2O}} = \frac{\left(\frac{\varepsilon}{n_{total}}\right)\left(\frac{1/2\,\varepsilon}{n_{total}}\right)^{1/2}}{\left(\frac{1-\varepsilon}{n_{total}}\right)} \quad (1.33)$$

$$n_{total} = n_{H_2} + n_{O_2} + n_{H_2O} = \varepsilon + 1/2\,\varepsilon + 1 - \varepsilon = 1 + 1/2\,\varepsilon \quad (1.34)$$

From NIST JANAF[4], at 2000 K, K_{H2O} (1/ $K_{f,H2O}$) of reaction (1.14) is equal to 0.00029 which is << 1; thus we expect mole fractions of products to be low. Solving for equilibrium yields using equations (1.33) and (1.34), we confirm that product yields are low; $\varepsilon = 0.0055$, $x_{H2} = 0.0055$, $x_{O2} = 0.00274$ and $x_{H2O} = 0.9912$. At higher temperatures, for example near where $K_{H2O} = 1$ ($T = 4300$ K), we see that conversion is much higher; $\varepsilon = 0.663$, $x_{H2} = 0.498$, $x_{O2} = 0.25$ and $x_{H2O} = 0.253$. In Figure 9 (right subplot), we show molar yields of all product species versus temperature for H_2O and CO_2 thermolysis reactions. Here, we have assumed that the only products that may be formed are H_2, CO and O_2[*]. As seen, the decomposition of CO_2 is expected to occur at more moderate temperatures than H_2O and is largely the result of the larger entropy change ($\Delta S°$) associated with decomposition which dictates the slope of the $\Delta G°$ curve versus temperature

[*] Practically, other products may form at higher temperatures, such as OH, O_3, etc. This calculation has limited the potential products only for simplicity in order to demonstrate the thermodynamic impact of Gibbs and equilibrium on the favorability of the gas splitting reactions.

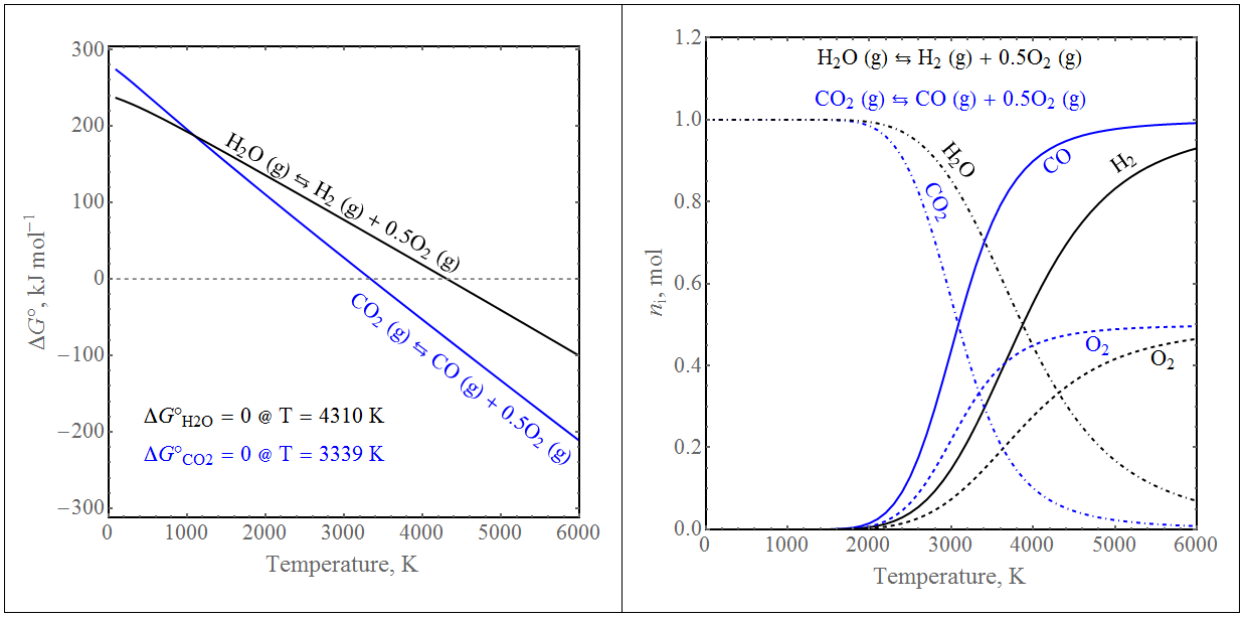

Figure 9. Left) $\Delta G°$ shown versus temperature for H_2O and CO_2 thermolysis reactions. Data extracted from NIST JANAF Thermochemical Tables. Right) Equilibrium yields of H_2O and CO_2 thermolysis reactions assuming only H_2, CO and O_2 may be produced.

($\Delta G^\circ = \Delta H^\circ - T\Delta S^\circ$). For more details regarding chemical reaction equilibria (especially multi-reaction equilibria) and determination of equilibrium yields refer to Smith and Van Ness[19] or another suitable thermodynamics textbook.

A Note on Thermolysis versus Electrolysis

For any chemical reaction, the total energy necessary to drive the reaction is equal to the standard reaction enthalpy ($\Delta H°$) which is usually only slightly dependent on temperature. Thus, when the reaction is driven at $\Delta G° = 0$, all of the energy supplied to the system is supplied as heat ($\Delta H° = T\Delta S° = Q$). However, if operation at lower temperatures is desired where $\Delta G°$ is positive and the reaction is not spontaneous, work (e.g. electrical, W_{el}, or mechanical work, W_{pv}) may be supplied to the system in addition to thermal energy ($\Delta H° = Q + W = Q + \Delta G°$) to shift the reaction equilibrium to the right side. Electrolysis of H_2O is perhaps the most ubiquitous and straightforward means of H_2O splitting and may be performed at room temperature where no thermal energy is supplied $\Delta H° \sim \Delta G° \sim W_{el}$, or elevated temperatures (High Temperature Electrolysis) where a mixture of thermal energy and electrical work is supplied. Because electrical work is usually derived from a thermal energy source, it is thermodynamically most attractive to use as much thermal energy as possible to drive the splitting of H_2O or CO_2. However, the elevated temperatures at which H_2O and CO_2 thermolysis are thermodynamically most attractive are prohibitively high (as discussed prior).

Iron Oxide Based Thermochemical Redox Cycles

The first realistic MeO cycle proposed was an iron oxide based redox cycle by Nakamura et al.[36] in 1977. The cycle is based on the stoichiometric reduction of magnetite (Fe_3O_4) to hematite (FeO), where Fe changes from the 3+ to 2+ oxidation state. Thus, the first step is the endothermic and solar driven reduction of magnetite to hematite and the subsequent release of gaseous oxygen, and the second step is the re-oxidation of hematite with H_2O (or CO_2) to produce H_2 (or CO).

Reduction: $\mathrm{Fe_3O_4} \xrightarrow{\Delta H_{Fe3O4}} 3\mathrm{FeO} + 1/2\,\mathrm{O_2(g)}$ (1.35)

Oxidation: $3\mathrm{FeO} + \mathrm{H_2O\,(g)} \xrightarrow{\Delta H_{ox}} \mathrm{Fe_3O_4} + \mathrm{H_2(g)}$ (1.36)

Thermodynamics of Iron Oxide Based Redox Cycles

While conceptually simple, the thermodynamics of these oxide systems are relatively complex, with a variety of different crystallographic and intermediate oxidation states existing between Fe_3O_4/FeO depending on the operating temperature and pressure[37-42]. However, for simplification purposes we will demonstrate the redox cycle here based only on the stoichiometric reaction, where the thermodynamics can be relatively easily described. The reduction of Fe_3O_4 may be seen as the sum of the reverse formation reaction of Fe_3O_4 and the formation reaction of FeO, as seen below, where the thermodynamics of each formation reaction are well documented[4].

$\mathrm{Fe_3O_4} \rightarrow 3\mathrm{Fe} + 2\mathrm{O_2(g)}$, $-\Delta H°_{f,Fe3O4}$ = 1120.89 kJ @ 298.15 K[4] (1.37)

$3\mathrm{Fe} + 3/2\,\mathrm{O_2(g)} \rightarrow 3\mathrm{FeO}$, $3\Delta H°_{f,FeO}$ = -816.13 kJ @ 298.15 K[4] (1.38)

Using the reaction coordinate method we can predict the equilibrium reduction extent of magnetite at a given temperature and pressure. To do so requires knowledge of either the Gibbs free energy or equilibrium constant of the reaction, which may then be related to the reaction coordinate by combining equations (1.25) , (1.26), (1.31) and (1.32) and knowing that $p_i = x_i P$, where P is the absolute pressure. Thus, we can show that:

$$K_{Fe3O4} = \exp\left(\frac{-\Delta G^{\circ}_{Fe3O4}}{RT}\right) = \frac{a_{FeO}{}^{3}\, p_{O_2}{}^{1/2}}{a_{Fe3O4}} = \left(\frac{1/2\,\varepsilon}{n_{total}}P\right)^{1/2} \quad (1.39)$$

This assumes unity activities of FeO and Fe_3O_4. $\Delta G°_{Fe3O4}$ may be determined by summing the Gibbs formation free energies of Fe_3O_4 and FeO ($\Delta G°_{f,Fe3O4}$ and $\Delta G°_{f,FeO}$). If knowledge of Gibbs formation free energies are not tabulated directly (as is common in NIST Chemistry WebBook) then these values may be determined from knowledge of the free energy function (FEF)[43] which mathematically is:

$$FEF\left(298\ \mathrm{K}\right) = \frac{G^{\circ}\left(T\right) - H^{\circ}\left(298\ \mathrm{K}\right)}{T} = \frac{H^{\circ}\left(T\right) - H^{\circ}\left(298\ \mathrm{K}\right)}{T} - S^{\circ}\left(T\right) \quad (1.40)$$

The Gibbs formation free energy is then related to FEF through the following relationship, for the reaction $\nu_1 E_1 + \nu_2 E_2 + \ldots = B$:

$$\frac{\Delta G_{f,B}\left(T\right)}{T} = FEF_{B}\left(298\ \mathrm{K}\right) - \sum_{i} \nu_i \left[FEF_{E_i}\left(298\ \mathrm{K}\right)\right] + \frac{\Delta H_{f,B}\left(298\ \mathrm{K}\right)}{T} \quad (1.41)$$

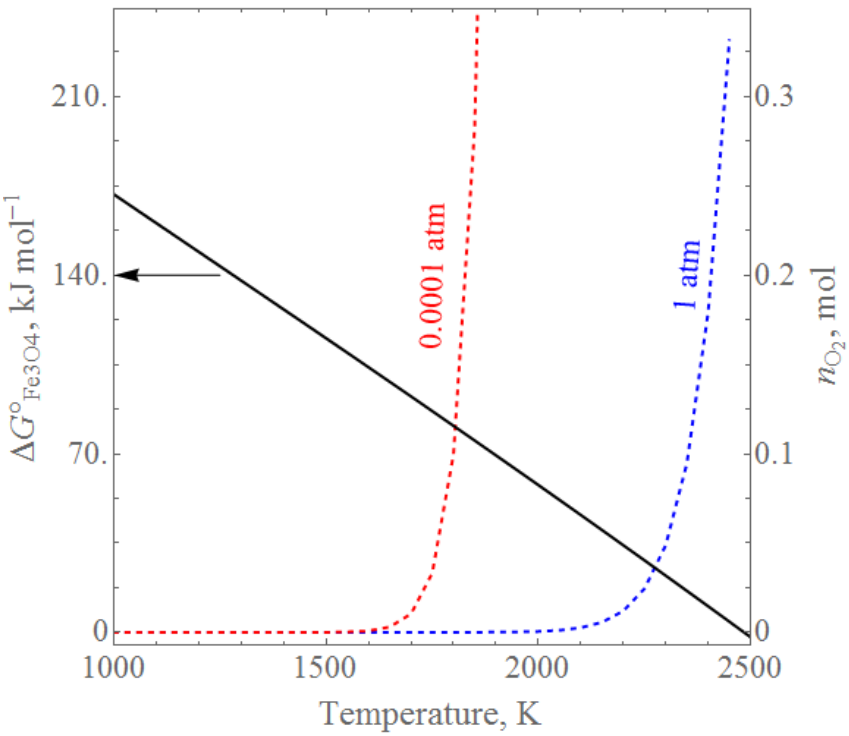

Figure 10. Standard Gibbs free energy change (left axis) for the reaction $Fe_3O_4 \rightarrow 3FeO+1/2O_2$. Also shown is the equilibrium gas phase O_2 on the right axis.

In Figure 10 we show the gas phase oxygen resulting from reduction of Fe_3O_4 to FeO as a function of temperature and two different total pressures. All thermodynamic data is derived from NIST Chemistry WebBook using polynomial fits but tabulated data is also available in NIST JANAF[4]. For these calculations a total pressure of 1 atm was assumed for the blue curve, $1x10^{-4}$ atm for the red curve. At 1 atm, gas phase oxygen does not increase appreciably until $\Delta G°_{Fe3O4}$ approaches zero, as expected. For example, at 2000 K where $\Delta G°_{Fe3O4}$ = 57.8 kJ mol^{-1}, n_{O2} equals $5x10^{-4}$ moles, but at 2450 K where $\Delta G°_{Fe3O4}$ approaches zero (4.2 kJ mol^{-1}), n_{O2} equals 0.33 moles. While this temperature is high, in practice it is alleviated by increasing the total number of gas phase species in the system (e.g. inert sweep gas) or decreasing the total pressure, as evidenced in the red curve where the reaction goes to completion near 1850 K when operating at $1x10^{-4}$ atm. This is especially important for the iron oxide system because of the fact that FeO melts at 1650 K, well below the decomposition temperature of Fe_3O_4 at ambient pressure. In fact, this low melting temperature is one of the reasons that this process has not been realized successfully in prototype solar reactors like other candidate materials such as CeO_2 (discussed below).

The oxidation reaction is simply the reverse of the reduction formation reactions summed with the thermolysis of H_2O. The reactions are shown below:

$$3Fe + 2O_2(g) \rightarrow Fe_3O_4 \text{ , } \Delta H°_{f,Fe3O4} = -1120.90 \text{ kJ @ 298.15 K}^4 \text{ (1.42)}$$

$$3FeO \rightarrow 3/2\,O_2(g) + 3Fe \text{ , } -3\Delta H°_{f,FeO} = 816.12 \text{ kJ @ 298.15 K}^4 \text{ (1.43)}$$

$$H_2O(l) \rightarrow 1/2O_2(g) + H_2(g) \text{ , } -\Delta H°_{f,H2O} = 285.83 \text{ kJ @ 298.15 K}^4 \text{(1.44)}$$

$$3FeO + H_2O\,(l) \rightarrow Fe_3O_4 + H_2(g) \text{ , } \Delta H_{GS} \text{ (Net Reaction)}$$

where the subscript GS in the bottom reaction (Net Reaction) enthalpy stands for Gas Splitting. To determine equilibrium compositions we may again turn to the reaction coordinate methodology and show that $\varepsilon = -(n_{H2O} - n_{H2O,i})$ and $\varepsilon = n_{H2}$, where it is assumed that there is no H_2 initially present in the system and the initial amount of H_2O is $n_{H2O,i}$. This assumes that all of the reactions above are in equilibrium (oxygen

partial pressure of each reaction is equivalent) and thus there is no net production of gas phase oxygen. Thus knowing either the formation equilibrium constants or Gibbs free energy formation energies, equilibrium H_2 product yields may be determined according to equations (1.45) and (1.46) below. Comparable calculations could be performed using CO_2 instead of H_2O[44].

$$K_{GS} = K_{Fe3O4}\frac{1}{K_{FeO}}\frac{1}{K_{H2O}} = \frac{x_{H2}}{x_{H2O}} = \frac{\varepsilon}{n_{H2O,i} - \varepsilon} \quad (1.45)$$

$$\Delta G_{GS} = \Delta G_{f,Fe3O4} - \Delta G_{f,FeO} - \Delta G_{f,H2O} = -RT\ln\frac{x_{H2}}{x_{H2O}} = -RT\ln\frac{\varepsilon}{n_{H2O,i} - \varepsilon} \quad (1.46)$$

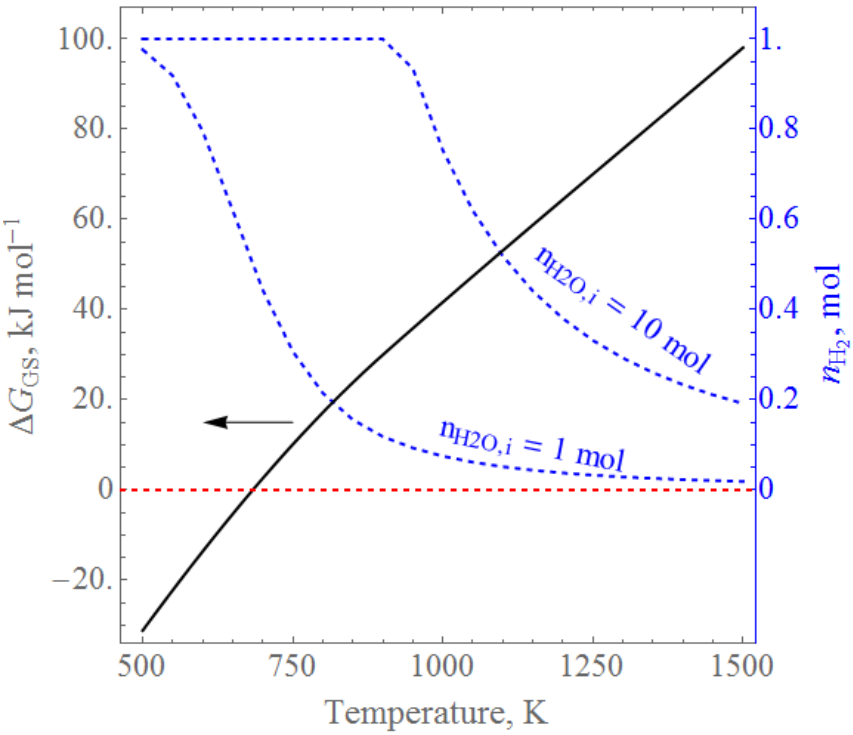

Figure 11. Equilibrium H_2 yields (blue dashed lines) resulting from H_2O dissociation as a function of oxidation temperature, alongside ΔG_{GS} (solid black curve), for the reaction $3FeO + H_2O\ (l) \rightarrow Fe_3O_4 + H_2\ (g)$. H_2 yields are shown for initial amounts of H_2O equal to 1 and 10 moles.

Shown in Figure 11 is the predicted equilibrium molar composition of H_2 per mol FeO and the Gibbs free energy change of the H_2O gas splitting reaction (ΔG_{GS}) versus oxidation temperature. As seen, ΔG_{GS} is negative for the lowest temperatures indicating that the oxidation reaction is thermodynamically favorable in this regime (K_{GS}>>1) but near 675 K ΔG_{GS} is equal to zero. As seen, for the lower temperature range the equilibrium H_2 yield approaches 1 (1 is indicitive of complete conversion) but at higher temperatures this decreases relatively quickly. If the amount of initial H_2O moles is increases from 1 to 10 however, the expected equilibrium H_2 yields are increased at higher temperatures. This doesn't come without a penalty however because all of the initial H_2O must be heated to the oxidation temperature of interest and the cost benefit of doing so relative to the gain in H_2 yields should be considered. This is discussed extensively in several thermodynamic analysis where solar-to-fuel conversion efficiencies are calculated over a wide range of operating conditions[45-48].

The trend of ΔG_{GS} with respect to temperature should be expected for all thermochemical redox materials; namely oxidation with H_2O or CO_2 is more favorable thermodynamically favorable at low temperatures. In this favorable regime, ΔG_{GS} is negative which implies that the Gibbs free energy of oxidation of the reduced oxide with oxygen ($3FeO + 0.5O_2 \rightarrow Fe_3O_4$) is more favorable than oxidizing H_2 with oxygen ($H_2 + 0.5O_2 \rightarrow H_2O$); effectively the reduced oxide wants the oxygen bound to the H_2O molecule more than H_2 does, and as a result the H_2O molecule is dissociated.

Practical Considerations of Iron Oxide Based Redox Cycles

One of the major issues associated with this cycle is the relatively low melting temperature of FeO, which occurs at 1650 K, below the temperature where the reduction reaction is conducted. As a result, severe sintering has been reported which typically limits the practicality of this process using pure magnetite[49-51]. To circumvent some of these issues, the materials are usually mixed with transition metals to form spinels (e.g. $NiFe_2O_4$, $CoFe_2O_4$)[42, 52, 53], are deposited on stabilizing supports[50, 54], or dissolved in ZrO_2 based oxides[55]. The incorporation of transition metals is known to reduce the reduction temperature from Fe^{3+} to Fe^{2+}, and are thus less likely to sinter upon formation of FeO. The dissolution into ZrO_2 based supports has been shown to enhance the reaction kinetics that are mostly bulk transport limited. This is because the oxygen exchange through ZrO_2 is much faster than Fe_3O_4[55].

Although thermodynamics dictates that the GS reaction is most favorable at the lowest temperature possible, there are other practical reasons why the reaction is usually driven at temperatures closer to 1000 K and sometimes only a few hundred degrees cooler than the reduction temperature (a typical reduction temperature range is on the order of 1673 to 1873 K depending on the material used, operating pressure, sweep gas flowrate, reduction extent, etc.). The primary reason has to do with chemical kinetics and solid state diffusion, which dictate the rate that a reaction will occur. For example, consider from experience the fact that iron is known to be relatively stable in air at ambient conditions, but the oxidation of iron with O_2 to form hematite (Fe_2O_3) is thermodynamically predicted at these conditions. The reason it does not oxidize readily (at least in the bulk) is because the reaction and diffusion rates are so slow at ambient. Only at higher temperatures where chemical kinetics and cation diffusion through the bulk are rapid enough does it begin to oxidize.

Another reason that oxidation temperatures are elevated has to do with the fact that redox cycles are operated between two temperature reservoirs, the hot reduction reactor and the cooler oxidation reactor. The cooler the oxidation reaction occurs, the more sensible heat will have to be added to the system to bring the reactants back to the reduction temperature. Here again there is a tradeoff between minimizing the temperature difference between reduction and oxidation temperatures, in order to decrease sensible heating requirements, and maximizing oxidation yields. In the case of both deposition on and dissolution of the oxide in supports, one must also consider the energy penalty associated with heating unreactive mass from the oxidation temperature to the reduction temperature. This has a negative impact on the overall efficiency and is widely considered not to be a practical solution to obtain high solar to fuel conversion efficiencies. To date, the CR5 is the only known solar reactor that has utilized iron oxide based materials and has been tested at the 16 kWth scale[56]. This reactor is unique compared to most in the sense that it has alternating, rotating rings of reacting material that effectively serve as a solid-solid heat exchanger with the goal of boosting efficiency.

In addition to the morphological changes that occur as a result of sintering, oxidation proceeds via an outwardly growing "shell" which can also present practical problems related to morphological variability with time. This is because oxidation proceeds via diffusion of cation species to the surface, rather than bulk oxygen, where they are oxidized.

Other Redox Cycles

There are a number of metal oxide redox pairs proposed in the literature that fall into one of two distinct classes of redox cycles – ***stoichiometric and nonstoichiometric***. Stoichiometric refers to the fact that the reduction of the oxide proceeds primarily from one distinct phase to another (e.g. $Fe_3O_4 \rightarrow 3FeO$); sometimes the transition is from one crystallographic phase to another or sometimes a complete change in

state of matter, from solid to vapor or liquid. As stated prior, iron oxide was the first stoichiometric metal oxide based cycle proposed but there have been several adaptations to this system through the introduction of other cations that are substituted for iron, so-call ferrites such as $CoFe_2O_4$[53, 54] and $NiFe_2O_4$[52]. In addition to iron oxide based cycles, ZnO[57, 58] and to a lesser extent SnO_2[59] cycles have been investigated that are based on the reduction of the oxide to a volatile metal (e.g $ZnO\ (s) \rightarrow Zn\ (g) + \frac{1}{2}O_2\ (g)$). The difficulty in these cycles lies in the production of the gaseous vapor products (Zn (g) or SnO (g)) that want to rapidly recombine with O_2 when the gas mixture is cooled. Thus, fairly elaborate quenching mechanisms or gas separation techniques must be employed to avoid recombination, similar to direct thermolysis of H_2O or CO_2. For a thorough discussion of stoichiometric cycles there are a host of review articles that the reader is referred to[12, 60-64].

Ceria-based Nonstoichiometric Redox Cycles

More recently, efforts have been focused on nonstoichiometric redox cycles in which there exist a spectrum of oxide oxidation states without undergoing a crystallographic or state of matter phase transition. Perhaps most understood and studied is the nonstoichiometric oxide ceria, or $CeO_{2-\delta}$, where δ refers to the nonstoichiometry of the oxide and is directly proportional to the average oxidation state of Ce in the oxide. Chueh *et al*. first proposed the use of this nonstoichiometric oxide cycle in which $CeO_{2-\delta}$ releases O_2 (g) during the reduction reaction that is proportional to its change in nonstoichiometry, or $\Delta\delta$ [*65]. Thus the reduction occurs according to the following reaction:

Reduction: $$CeO_{2-\delta i} \xrightarrow{\Delta H_{rxn}} CeO_{2-\delta f} + \frac{\delta_i - \delta_f}{2} O_2(g) \quad (1.47)$$

Where δ_i is and δ_f are the initial and final nonstoichiometries prior to and following reduction. The oxidation reaction to split H_2O or CO_2 proceeds as expected according to

Oxidation: $$CeO_{2-\delta f} + (\delta_i - \delta_f) H_2O \xrightarrow{\Delta H_{GS}} CeO_{2-\delta i} + (\delta_i - \delta_f) H_2 \quad (1.48)$$

Thermodynamics of Ceria-based Nonstoiciometric Redox Cycles

The nonstoichiometry of ceria is strongly dependent on temperature and oxygen partial pressure and has been studied in detail by several authors, and is documented nicely by Panlener *et al*.[66] The advantage of ceria based systems compared to other stoichiometric systems such as iron oxide is that $CeO_{2-\delta}$ is extremely stable, both morphologically and crystallographically, over a wide temperature range and therefore is not as affected by sintering and subsequent deactivation[44, 67, 68]. Further kinetics are extremely rapid compared to the iron oxide system due to the high ambipolar oxygen diffusion rates in the bulk, which is dictated by its high ionic and electronic conductivities[44]. Because oxygen is the primary species that is transported in the bulk, growing scales also are not formed like in the iron-oxide based systems. Oxygen nonstoichiometry of ceria as a function of temperature and oxygen partial pressure, as measured by Panlener et al. in a thermogravimetric analyzer[66], are shown in Figure 12. As seen, δ increases with increasing temperature and decreasing oxygen partial pressure.

Ceria Reduction

Thermodynamic data of nonstoichiometric systems such as ceria is not as readily tabulated like that for iron oxide and other stoichiometric reactions. However, it may be easily extracted from measured nonstoichiometry data such as that shown below. For this, an infinitesimally small change in nonstoichiometry is considered, as shown below:

[*] It should be noted that Flamant *et al*. proposed the use of a ceria based cycle prior to Chueh *et al*. but in that work they proposed reducing all the way to the Ce_2O_3 phase.

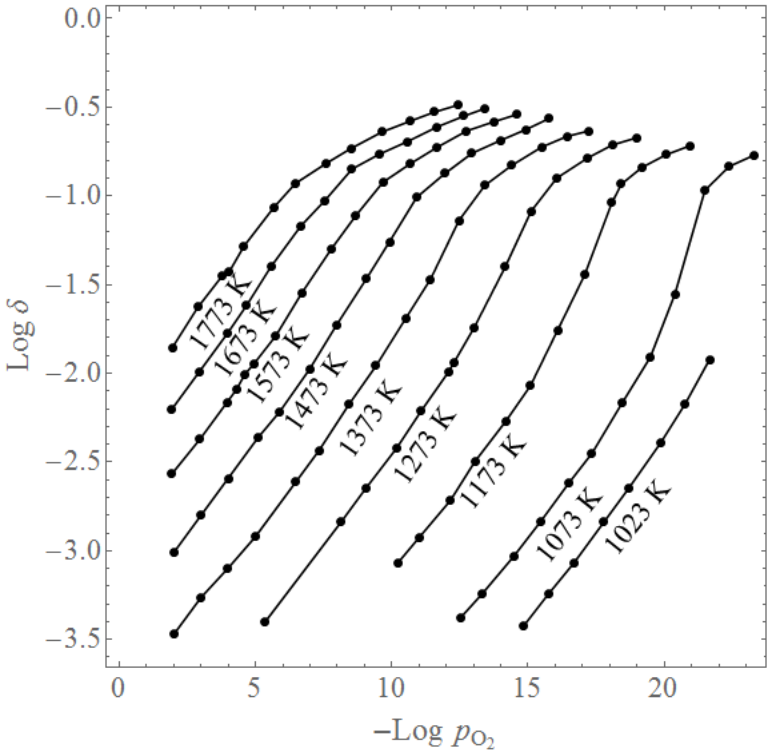

Figure 12. Ceria ($CeO_{2-\delta}$) oxygen nonstoichiometry shown as a function of p_{O2} for temperatures between 1023 K to 1773 K. Data is taken from Panlener *et al.*[63]

$$\lim_{\delta_f - \delta_i = 0} \frac{1}{\delta_i - \delta_f} CeO_{2-\delta_i} \rightarrow \frac{1}{\delta_i - \delta_f} CeO_{2-\delta_f} + \tfrac{1}{2} O_2(g) \quad (1.49)$$

Assuming that the activity of the solid reactants and products in the above reaction are the same, it can be shown that

$$\Delta g_O(\delta, T) = -RT \ln p_{O_2}(\delta, T)^{1/2} \quad (1.50)$$

where Δg_o is the partial molar Gibbs free energy which is a function of both nonstoichiometry and temperature[44, 66, 69]. Δg_o may be related to the partial molar enthalpy (Δh_o) and partial molar entropy (Δs_o) through the well-known relation

$$\Delta g_O(\delta, T) = \Delta h_O(\delta) - T\Delta s_O(\delta) \quad (1.51)$$

And upon rearrangement of equations (1.50) and (1.51) it can be shown that

$$\ln p_{O_2}(\delta, T)^{1/2} = -\left(\frac{1}{T}\right)\frac{\Delta h_O(\delta)}{R} + \frac{\Delta s_O(\delta)}{R} \quad (1.52)$$

Thus, the slope of a plot of $\ln p_{O2}^{1/2}$ versus inverse temperature (at a constant nonstoichiometry) is proportional to Δh_o and the intercept is proportional to Δs_o. When acquiring data like that in Figure 12 above, it is important to obtain enough data points at different temperatures and oxygen partial pressures at

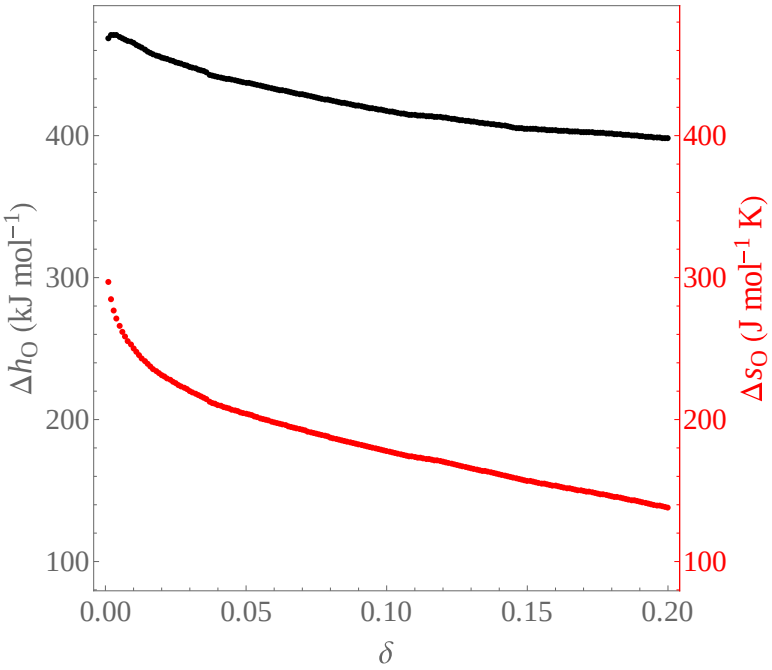

Figure 13. Partial molar enthalpy (Δh_o) and entropy (Δs_o) plotted as a function of δ in $CeO_{2-\delta}$. Nonstoichiometry equilibrium data obtained from Panlener *et al*.[63]

a fixed delta (effectively a horizontal cross-section through the plot) to give confidence to the fitted data (e.g more than two points). Results for Δh_o and Δs_o using experimental nonstoicheometry data obtained from Panlener *et al*. are shown in Figure 13. As seen, enthalpy decreases with increasing nonstoichiometry from about 480 to 400 kJ mol^{-1} as δ increases from 0 to 0.2. Entropy also decreases with increasing nonstoichiometry but even more strongly than enthalpy; it decreases form about 300 J mol^{-1} K^{-1} to 150 J mol^{-1} K^{-1} as δ increases from 0 to 0.2. Once Δh_o and Δs_o are known as a function of nonstoichiometry it is then possible to calculate predicted oxygen partial pressures or nonstoichiometries for reduction conditions by using one of the two as an input alongside temperature using equation (1.52).

Example Question 1:

Given ceria at 1773K in an environment with an oxygen partial pressure of 10^{-5} atm, calculate the oxygen non-stoichiometry (δ) at equilibrium using an iterative, guess and check, approach.

Solution 1:

The question states that a sample of ceria has a temperature of 1773K and exists in an environment with an oxygen partial pressure (p_{O2}). The oxygen non-stoichiometry of ceria can be found as a function of these two properties by relating the two well-known equations for partial molar Gibbs free energy, Equations 1.50 and 1.51.

$$\Delta g_o(\delta,T) = -RT\ln p_{O_2}(\delta,T)^{1/2} \quad (1.50)$$

$$\Delta g_o(\delta,T) = \Delta h_o(\delta) - T\Delta s_o(\delta) \quad (1.51)$$

Equating these two relationships and dividing by T, we arrive at equation 1.52.

$$\ln p_{O_2}(\delta,T)^{1/2} = -\left(\frac{1}{T}\right)\frac{\Delta h_o(\delta)}{R} + \frac{\Delta s_o(\delta)}{R} \quad (1.52)$$

Here, the left side of the equation can be directly calculated, and values for temperature (T) and the universal gas constant (R) can be plugged in to reach an easily iterated equation.

$$-5.756 = -\left(\frac{1}{1773\text{K}}\right)\frac{\Delta h_o(\delta)}{8.314\frac{\text{J}}{\text{mol·K}}} + \frac{\Delta s_o(\delta)}{8.314\frac{\text{J}}{\text{mol·K}}}$$

Using an initial guess of the oxygen non-stoichiometry (δ), refer to data obtained from Panlener *et al.* in Figure 13 to retrieve enthalpy and entropy values. Then calculate the right-hand side (RHS) of the equation and compare to the left-hand side (LHS).
Initial guess will be taken as: δ = 0.05
(RHS) = -5.399
Second guess will be δ = 0.055
RHS = -5.706
Continuing iterations until RHS = LHS will converge on the exact answer of δ = 0.0589

Note: In order to obtain accurate values of enthalpy and entropy, it is often useful to fit a polynomial curve to the data found in Figure 13 and use your favorite mathematical software to calculate the respective values based on your guess of oxygen non-stoichiometry.

Example Question 2:

Given ceria at 1773K in an environment with an oxygen partial pressure of 10^{-5} atm, calculate the oxygen non-stoichiometry (δ) at equilibrium by employing a minimization technique using your favorite mathematical software.

Solution 2:

Note: This solution will employ MATLAB to solve for oxygen non-stoichiometry (δ)

The question provides that a sample of ceria has a temperature of 1773K and exists in an environment of oxygen partial pressure (Po_2). The oxygen non-stoichiometry of ceria can be found as a function of these two properties by relating the two well-known equations for partial molar Gibbs free energy, Equations 1.50 and 1.51, and arriving at Equation 1.52 using the same method as seen in Solution 1.

$$\ln p_{O_2}(\delta,T)^{1/2} = -\left(\frac{1}{T}\right)\frac{\Delta h_o(\delta)}{R} + \frac{\Delta s_o(\delta)}{R} \qquad (1.52)$$

In this solution, the MATLAB function "fzero" will be used to search for a non-stoichiometry that will satisfy the following version of Equation 1.52, where all terms have been rearranged to equal zero.

$$\ln p_{O_2}(\delta,T)^{1/2} + \left(\frac{1}{T}\right)\frac{\Delta h_o(\delta)}{R} - \frac{\Delta s_o(\delta)}{R} = 0$$

Before using the fzero solver, functions for changes in enthalpy and entropy as a function of oxygen non-stoichiometry should be defined. This can be done in several ways including fitting a polynomial to existing data or using existing data with an interpolating function. In the blocks of code seen in this solution, these functions are dH(x) and dS(x).

The fzero function takes an input of a function (f) and an initial guess (x) in the format fzero(f,x)
An example of code employing this technique is seen below, along with the MATLAB output of the answer, delta = 0.0589.

```
>> T=1773; Po2=1e-05; R=8.314;

>> f=@(x)log(Po2^0.5)+((1/T)*(dH(x)/R))-(dS(x)/R);

>> delta=fzero(f,0.05)

        delta = 0.0589020711130001
```

Note: Using simple coding loops in MATLAB or another software, this minimization technique can be employed across a range of conditions to reproduce the data seen in Figure 12.

Example Question 3:

Compute change in partial molar entropy and change in partial molar enthalpy as a function of oxygen non-stoichiometry for ceria.

Solution3:

In order to calculate the change in entropy and change in enthalpy of ceria at a given condition, one must recall Equation 1.52.

$$\ln p_{O_2}(\delta,T)^{1/2} = -\left(\frac{1}{T}\right)\frac{\Delta h_o(\delta)}{R} + \frac{\Delta s_o(\delta)}{R} \qquad (1.52)$$

Comparing this equation to slope-intercept form, $y = mx + b$, it can be seen that by plotting the natural log of the square root of oxygen partial pressure on the vertical axis and the reciprocal of temperature on the horizontal axis, the slope of the resulting plot will be proportional to the change in enthalpy and the vertical axis intercept will be proportional to the change in entropy, at a fixed nonstoichiometry.

Using data such as that presented in Figure 12 (obtained experimentally), oxygen partial pressure values for each isotherm at a range of constant delta values should be tabulated. This will result in a data set that can be easily converted to represent $\ln p_{O_2}(\delta,T)^{1/2}$. For example, for δ = 0.01 the data looks like the following:

$\ln p_{O_2}(\delta,T)^{1/2}$	-3.256	-5.313	-7.884	-10.570	-13.827	-17.598	-21.997	-24.569
1/T	5.98E-4	6.37E-4	6.79E-4	7.28E-4	7.86E-4	8.52E-4	9.32E-4	9.78E-4

Note that data is not measured for the highest temperature at 1773 K for this nonstoichiometry.

Plotting the $\ln p_{O_2}(\delta,T)^{1/2}$ against $\left(\frac{1}{T}\right)$ should be linear with a negative slope for each constant delta value, as shown below.

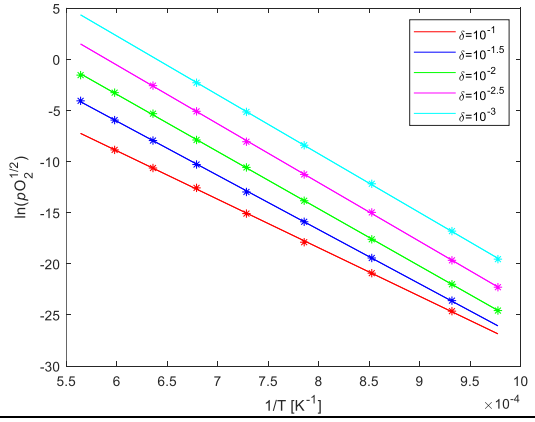

Calculating the slope of each line will result in $\frac{\Delta h_o(\delta_i)}{R}$ where δ_i is one constant delta value. The respective y-intercepts will correspond to $\frac{\Delta s_o(\delta_i)}{R}$. Scaling these values by the universal gas constant (R), in this case equal to 8.314 kJ mol^{-1} K^{-1} and plotting them against a range of deltas will result in the plot seen in Figure 13 that shows partial molar enthalpy and partial molar entropy as a function of oxygen non-stoichiometry.

Ceria Oxidation with H_2O (or CO_2)

During oxidation with H_2O, the following reactions occur.

$$\frac{1}{\delta_i - \delta_f}\mathrm{CeO}_{2-\delta_f} + \tfrac{1}{2}\mathrm{O}_2(g) \rightarrow \frac{1}{\delta_i - \delta_f}\mathrm{CeO}_{2-\delta_i},\ -\Delta g_O\,(T,\delta) \quad (1.53)$$

$$\mathrm{H_2O}(l) \rightarrow \tfrac{1}{2}\mathrm{O_2}(g) + \mathrm{H_2}(g) \quad (1.54)$$

This results in the net oxidation reaction proceeding according to

$$\frac{1}{\delta_i - \delta_f}\mathrm{CeO}_{2-\delta_f} + \mathrm{H_2O}\ (l) \rightarrow \frac{1}{\delta_i - \delta_f}\mathrm{CeO}_{2-\delta_i} + \mathrm{H_2}(g),\ \Delta G_{ox} \quad (1.55)$$

A qualitative indicator of oxidation thermodynamic favorability may be seen by comparing the magnitudes of $-\Delta g_O$ (equation 1.53) and $\Delta G°_{f,H2O}$ (reverse of equation 1.54). By doing so, the thermodynamic favorability of either nonstoichiometric ceria or H_2 to consume gaseous O_2 may be discerned. These quantities are plotted below in Figure 14 in blue lines for δ_i = 0.001, 0.01 and 0.1. Also plotted in red lines are the Gibbs free energy change (ΔG_{ox}) of the net oxidation reaction, equation (1.55). As seen, the slope of each of the $-\Delta g_O$ lines is greater than $\Delta G°_{f,H2O}$ which is one criteria necessary for thermochemical redox cycles, as discussed in the section above entitled "Thermochemical Redox Cycles". The temperature where $-\Delta g_O$ crosses $\Delta G°_{f,H2O}$ (a second criteria, resulting from a larger enthalpy change) increases with increasing δ_i, which indicates that the reaction from δ_f to that specific nonstoichiometry is possible at increasingly higher temperatures. Put another way, to oxidize to lower δ_i where oxidation conversions are greater (δ_f - δ_i), the temperature should be as low as possible. For δ_i decreasing from 0.1 to 0.001, the temperatures that this intersects $\Delta G°_{f,H2O}$ are 1386 K, 1115 K and 912 K, respectively. As seen in the red curves, ΔG_{ox} is negative below each of these respective temperatures, indicating their favorability. Also note that nearly complete oxidation to 0.001 is favorable below 912 K, compared to ~675 K for FeO oxidation to Fe_3O_4 (c.f. Figure 11), meaning that reduced ceria should oxidize more readily at higher temperatures, which is beneficial from a kinetic and efficiency perspective.

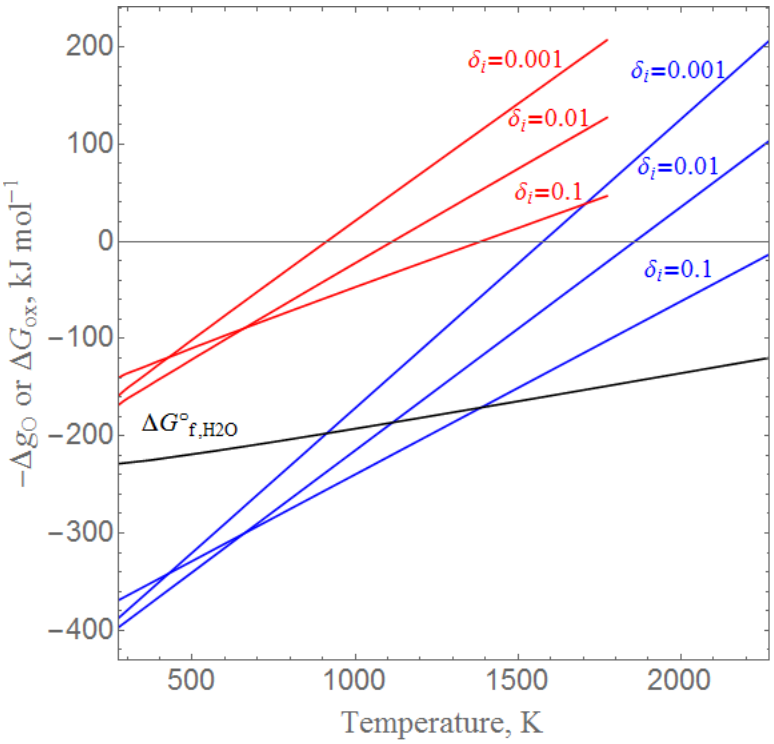

Figure 14. Partial molar Gibbs free energy change for the ceria oxidation reaction, $-\Delta g_O$ (blue), Gibbs free energy change of the water formation reaction, $\Delta G°_{f,H2O}$ (black) and Gibbs free energy change for the oxidation of ceria with H_2O, ΔG_{ox} (red), all as a function of temperature. δ_i refers to the nonstoichiometry in ceria, $CeO_{2-\delta i}$, following oxidation.

The approach used to determine oxidation yields is similar to that discussed prior for iron oxide, but instead of oxide formation energies, partial molar properties are used. It is assumed that reactions (1.53) and (1.54) above are in equilibrium and thus the oxygen partial pressures are equal. Therefore, combining equations (1.50) and (1.27) we can show that

$$\Delta g_O\left(\delta_i, T\right) = -RT \ln \frac{K_{H2O}\, p_{H2O}}{p_{H2}} \quad (1.56)$$

Assigning reaction coordinates as discussed prior we can relate the partial pressures to moles of each species at equilibrium to show the following.

$$\Delta g_O\left(\delta_i, T\right) = -RT \ln \frac{K_{H2O}\left(n_{H2O,i} - \varepsilon\right)}{\varepsilon} \quad (1.57)$$

where

$$\varepsilon = \delta_f - \delta_i \quad (1.58)$$

Therefore, the reaction coordinate can be solved iteratively using equation (1.57). Results for H_2 yields are shown in Figure 15 as a function of temperature. Here, the total pressure was kept constant at 1 atm, δ_f was fixed at 0.1 (following reduction), and $n_{H2O,i}$ was set to δ_f, $10\delta_f$ and $100\delta_f$. When $n_{H2O,i} = \delta_f$, oxidation is nearly 100% complete (mol $H_2 = \delta_f$) for temperatures lower than 800 K, reaches 90% completion at about 1019 K and then steadily decreases with increasing temperature; only 10% completion is reached at 1596 K. For larger amounts of initial H_2O in the system, oxidation extents are greater at higher temperatures, as one would expect from Le Chatlier's principle. For example, when $n_{H2O,i} = 100\delta_f$, oxidation is nearly 100% complete at 1200 K and lower. 90% completion is achieved at 1396 K and 10 % at 2529 K (outside scale of figure). While at first glance this may appear to be a convenient way to increase oxidation yields, the conversion of H_2O to H_2 should be considered because of sensible heating requirements necessary to bring

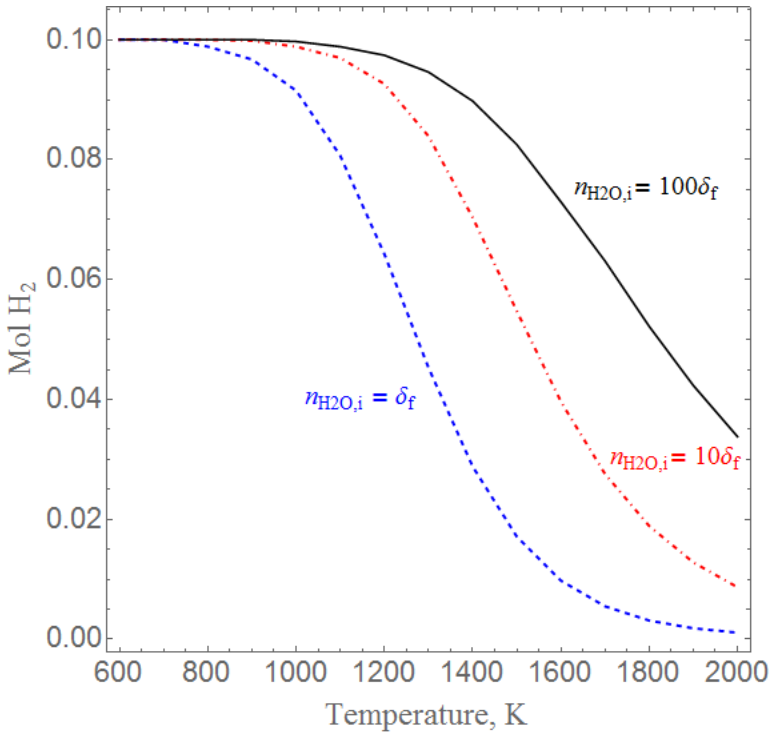

Figure 15. H_2 produced as a result of oxidation of $CeO_{2-\delta f}$ with H_2O. Total pressure is kept constant at 1 atm and δ_f is set 0.1. The same general trends hold for different values of δ_f.

the excess H_2O to the oxidation temperature. Here, conversion (α) is defined as the moles of water converted to H_2 divided by the total amount of water introduced into the system, shown mathematically as.

$$\alpha = \frac{n_{H2O,i} - n_{H2O}}{n_{H2O,i}} \quad (1.59)$$

When $n_{H2O,i} = \delta_f$, conversion is the same as oxidation completion described prior. However, when $n_{H2O,i} = 100\delta_f$, conversion will always be << 100% because the amount of H_2O introduced into the system is much larger than the total number of moles that may react to produce H_2. Thus, at the conditions considered prior (1200 K, 1396 K and 2529 K), conversion is only 1%, 0.9% and 0.1%. The importance of conversion becomes apparent when comparing the magnitudes of enthalpies of heating H_2O to the oxidation temperature of interest relative to the higher heating value of H_2. For example, consider oxidation at 1396 K where $n_{H2O,i} = 100\delta_f$, and conversion is equal to 0.9%.This implies that 10 mol of H_2O must be heated and 0.09 mol of H_2 is produced. The enthalpy required to heat 10 mol of H_2O from ambient conditions to 1396 K is 870.3 kJ, while the HHV is only 25.7 kJ.

If the goal is to dissociate CO_2 rather than H_2O, similar calculations can be performed using the reaction coordinate methodology. For CO_2 splitting it is important to consider that C (s) may be thermodynamically predicted rather than CO (g). Nevertheless, this has not been observed experimentally and it is typical to only consider the $CO_2 \rightarrow CO + ½\ O_2$ reaction.

Example Question 4:

Given data arrays of Δh_o (kJ/mol) and Δs_o (J/mol $*$ K) versus δ for Ceria, fit a third degree poynomical function suitable for describing Δh_o and Δs_o as a function of δ using the *curve*fit_ function from the *scipy.optimize* library.

Solution 4:

Note: For this we will use Python and import tabulated data from a *.csv* file.

```
In [1]:   #Import necessary libraries and data arrays from files.
          import numpy as np
          import pandas as pd
          delta_h = pd.read_csv('Change_in_EnthalpyVSDelta.csv',
          names=['delta','$\Delta h_o$ (kJ/mol)'])
          delta_s = pd.read_csv('Change_in_EntropyVSDelta.csv',
          names=['delta','$\Delta s_o$ (J/mol*K)'])
          delta_h.head()
Out[1]:
```

	delta	Δh_o (kJ/mol)
0	0.006319	472.083
1	0.011813	465.863
2	0.016758	461.339
3	0.021703	455.685
4	0.026374	452.292

Plot extracted data by slicing the data array in different columns. The first column represents δ and the second column represents either Δh_o or Δs_o

```
In [2]:   #Import necessary libraries and plot raw data for better visualization
          import matplotlib.pyplot as plt
          plt.plot(delta_h.iloc[:,0], delta_h.iloc[:,1], 'bo', markersize=3, label
          ='$\Delta h_o$ data')
          plt.plot(delta_s.iloc[:,0], delta_s.iloc[:,1], 'gs', markersize=3, label
          ='$\Delta s_o$ data')
          plt.xlabel('$\delta$')
          plt.ylabel('$\Delta h_o$'+' (kJ $mol^{-1})$'+' , '+'$\Delta s_o$'+' (J $
          mol^{-1}K^{-1})$')
          plt.legend(loc='best')
          plt.ylim(0,500)
          plt.title('Enthalpy and Entropy versus Delta')
          plt.show()
```

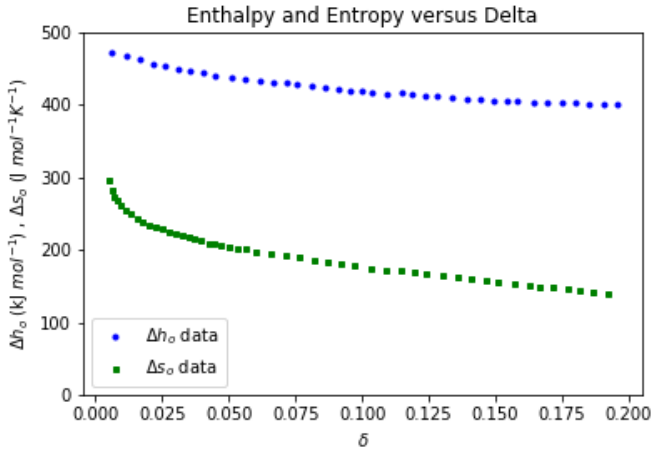

Define a polynomial function *poly* dependent on delta (**d**) and the different coefficients of the polynomial (**c1,c2,c3,c4**)

```
In [3]:    def poly(d,c1,c2,c3,c4):
               return c1*d**3+c2*d**2+c3*d+c4
```

```
In [4]:    #Import necessary libraries and calculate the polynomial coefficients
           from scipy.optimize import curve_fit
           coeff1, pcov = curve_fit(poly, delta_h.iloc[:,0], delta_h.iloc[:,1])
           coeff2, pcov = curve_fit(poly, delta_s.iloc[:,0], delta_s.iloc[:,1])
           print('Coefficients for delta_h : ', coeff1)
           print('Coefficients for delta_s : ', coeff2)
```

```
           Coefficients for delta_h :  [-8899.81954683  4542.24540679  -943.4535872
           3   475.59544598]
           Coefficients for delta_s :  [-48944.72003456  17642.77453637  -2368.8771
           4186    284.14274668]
```

Plot curve fit polynomial function *poly* with the obtained coefficients along with the previously plotted raw data to show comparison

```
In [5]:    d_fit = np.arange(0,0.2,0.001)  #Define new array for d
           plt.plot(d_fit, poly(d_fit, *coeff1), 'r', label='$\Delta h_o$ curve fit
           ')
           plt.plot(d_fit, poly(d_fit, *coeff2), 'k', label='$\Delta s_o$ curve fit
           ')
           plt.plot(delta_h.iloc[:,0], delta_h.iloc[:,1], 'bo', markersize=3, label
           ='$\Delta h_o$ data')
           plt.plot(delta_s.iloc[:,0], delta_s.iloc[:,1], 'gs', markersize=3, label
           ='$\Delta s_o$ data')
           plt.xlabel('$\delta$')
           plt.ylabel('$\Delta h_o$'+' (kJ $mol^{-1})$'+' , '+'$\Delta s_o$'+' (J $
           mol^{-1}K^{-1})$')
           plt.legend(loc='best', ncol=2)
           plt.ylim(0,500)
           plt.title('Enthalpy and Entropy versus Delta with Curve Fit')
           plt.show()
```

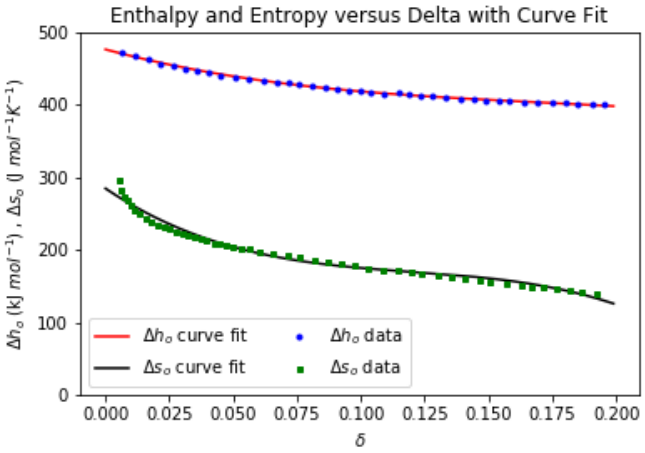

Solution: Δh_o and Δs_o can now be computed as a function of δ and the curve fit coefficients found, *coeff1* and *coeff2* respectively.

Example Question 5:

Given a temperature of operation $T = 1273$ K for ceria and an initial amount of moles of water $n_{\mathrm{H2O,i}} = \delta_{\mathrm{f}} = 0.1$. Solve for δ_{i} using an iterative approach.

Background: The partial molar Gibbs free energy for Ceria Δg_{o}, which is a function of both nonstoichiometry and temperature, is expressed as two equations below:

$$\Delta g_{\mathrm{o}}(\delta, T) = -\mathrm{R}T \ln p_{\mathrm{O}_2}(\delta, T)^{1/2} \qquad (1.50)$$

$$\Delta g_{\mathrm{o}}(\delta, T) = \Delta h_{\mathrm{o}}(\delta) - T\Delta s_{\mathrm{o}}(\delta) \qquad (1.51)$$

Also, the oxygen partial pressure p_{O_2} can be obtained from the reaction equilibrium analysis of the dissociation of H_2O. From (1.33) we recognize that the reaction coordinate ε is equal to $\delta_{\mathrm{f}} - \delta_{\mathrm{i}}$,

$$K_{\mathrm{H_2O}} = \frac{\left(\frac{\epsilon}{n_{\mathrm{total}}}\right) * p_{\mathrm{O}_2}^{1/2}}{\left(\frac{n_{\mathrm{H2O,i}} - \epsilon}{n_{\mathrm{total}}}\right)} = \frac{(\delta_{\mathrm{f}} - \delta_{\mathrm{i}}) * p_{\mathrm{O}_2}^{1/2}}{n_{\mathrm{H2O,i}} - (\delta_{\mathrm{f}} - \delta_{\mathrm{i}})}$$

$$p_{\mathrm{O}_2}^{1/2} = \frac{K_{\mathrm{f,H2O}} * \left[n_{\mathrm{H2O,i}} - (\delta_{\mathrm{f}} - \delta_{\mathrm{i}})\right]}{(\delta_{\mathrm{f}} - \delta_{\mathrm{i}})}$$

Solution 5:

Note: For this we will use Python, and import data for the equilibrium constant of formation of water $K_{f,H2O}$ from the NIST-JANAF website. A curve fitting procedure needs to be applied, similar to Example Question 4.

In [6]:
```
#Import Equilibrium Constant Data for formation of Water, 1bar, (l,g)
Kf_H2O = pd.read_csv('H2O_Equilibrium_Constant.csv', names=['Temperature
(K)','log $K_f$'])
Kf_H2O.head()
```

Out[6]:

	Temperature (K)	log K_f
0	280.00	44.796
1	298.15	41.546
2	300.00	41.237
3	320.00	38.131
4	340.00	35.396

The data has a linear relationship when plotted versus $1/T$ on the x-axis.

In [7]:
```
#Plot raw data for better visualization
plt.plot(1/(Kf_H2O.iloc[:,0]), Kf_H2O.iloc[:,1], 'bo', markersize=3, lab
el='$K_f$ data')
plt.xlabel('$1/T$'+' (K)')
plt.ylabel('log '+'$K_f$')
plt.title('Equilibrium Constant for Formation of Water')
plt.legend()
plt.show()
```

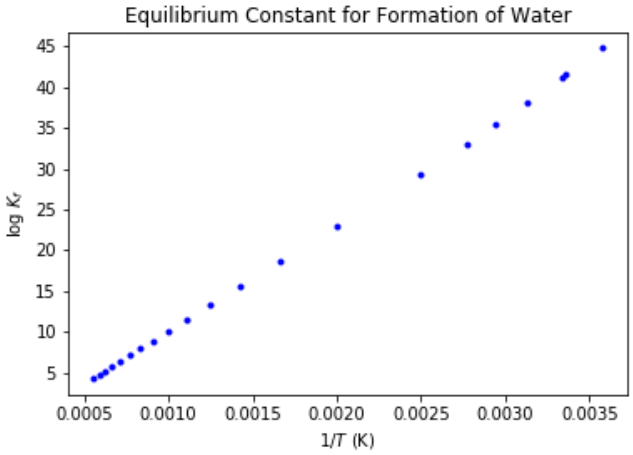

Define a function named *linear* dependent on the **(x)**, the slope **(m)** and the y-intercept **(b)**. Calculate the *linear* function coefficients. Then, plot the curve fit function *linear* with the obtained coefficients along with the previously plotted raw data to show comparison.

In [8]:
```
def linear(x, m, b):
    return m*x+b
```

In [9]:
```
#Calculate the linear function coefficients in the same way as Example Question 4
coeff3, pcov = curve_fit(linear, 1/(Kf_H2O.iloc[:,0]), Kf_H2O.iloc[:,1])
print('Coefficients for Kf : ', coeff3)
```

```
Coefficients for Kf :  [ 1.32377167e+04 -3.21602829e+00]
```

In [10]:
```
x_fit = np.arange(0,0.0035,0.00005)  #Define new array for x
plt.plot(1/(Kf_H2O.iloc[:,0]), Kf_H2O.iloc[:,1], 'bo', markersize=3, label='$K_f$ data')
plt.plot(x_fit, linear(x_fit, *coeff3), 'r', label='$K_f$ curve fit')
plt.xlabel('$1/T$'+' (K)')
plt.ylabel('log '+'$K_f$')
plt.title('Equilibrium Constant for Formation of Water with Curve Fit')
plt.legend()
plt.show()
```

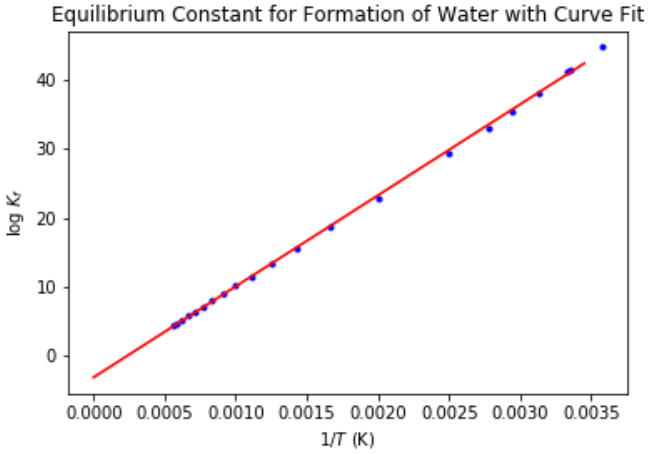

Define functions for the partial molar Gibbs free energy as a function of both nonstoichiometry and temperature, make sure to replace the expression for oxygen partial pressure into(1.50). δ_i is represented as d.

```
In [11]:  #Define variables and fixed parameters
          R = 0.008314  #(kJ/mol K)
          T = 1273  #(K)
          d_f = 0.1  #(moles)
          n_H2O = df  #(moles)

In [12]:  def Gibbs1(d):
              return -R*T*np.log((n_H2O-(d_f-d))/((d_f-d)*10**(linear((1/T),
          *coeff3))))
          def Gibbs2(d):
              return poly(d, *coeff1)-poly(d, *coeff2)*T/1000
```

Trial and error approach. Iteratively input values for delta such that $0.0 < \delta_i < \delta_f$. Modify values in both functions until the result is approximately the same. If we substract both functions the value should get close to zero when the function values are the same.

```
In [13]:  #Try d=0.08
          attempt = Gibbs1(0.08)-Gibbs2(0.08)
          print(attempt)

          -31.955065691423272

In [14]:  #Try d=0.09
          attempt = Gibbs1(0.09)-Gibbs2(0.09)
          print(attempt)

          -42.389362187631036

In [15]:  #Try d=0.06
          attempt = Gibbs1(0.06)-Gibbs2(0.06)
          print(attempt)

          -14.49090419841059

In [16]:  #Try d=0.045
          attempt = Gibbs1(0.045)-Gibbs2(0.045)
          print(attempt)

          1.4560637768568085
```

Solution: $\delta_i = 0.045$ approximately.

Example Question 6:

Given a temperature of operation $T = 1273$ K for Ceria and an initial amount of moles of water $n_{H2O,i} = \delta_f = 0.1$. Solve for δ_i and the H_2 yield. Create a solver/minimizer using the *minimize* function from the *scipy.optimize* library.

Solution 6:

Note: For this we will use Python, and remember that $H_2 = \delta_f - \delta_i$, which is the difference between the final and initial nonstoichiometries.

Define the function *objective* , which is the absolute value of the difference between both partial molar Gibbs free energy expressions, in that way we guarantee the result gets as close possible to zero. δ_i is represented as d.

```
In [17]: #Import necessary libraries for minimization procedure and define object
         ive function to minimize
         from scipy.optimize import minimize
         def objective(d):
             return np.abs(poly(d,*coeff1)- poly(d,*coeff2)*T/1000+(R*T*np.log((n
         _H2O-(d_f-d))/((d_f-d)*10**(linear((1/T),*coeff3))))))
```

The minimization method we are using, **(SLSQP)**, requires a set of initial guesses and boundaries for every value. Define those parameters, then minimize the *objective* function.

```
In [18]: initial_guess = 0.01
         solution = minimize(objective, initial_guess, method='SLSQP', tol=1e-10,
         options={'disp': False}, bounds=[(0,0.2)])
         print('Value of delta_i is: %.4f' %solution.x[0])

         Value of delta_i is: 0.0462


In [19]: print('H_2 yield is: %.4f' %(df-solution.x[0]))

         H_2 yield is: 0.0538
```

Solution: $\delta_i = 0.0462$ and $H_2 = 0.0538$.

Example Question 7:

Given six different temperatures of reduction $T_{\mathrm{H}} = 1573,1673,1773,1873,1973,2073$ K, temperature of oxidation $800\ \mathrm{K} < T_{\mathrm{L}} < 1200$ K, and oxygen partial pressure $p_{O_2} = 10^{-5}$ atm for Ceria. Compute H_2 yield to reproduce data from Chueh et al. **Figure 17.a[44].**

Solution 7:

Note: For this we will use Python, and remember that $n_{\mathrm{H2O,i}} = \delta_{\mathrm{f}}$ (initial moles of water are equal to the nonstoichiometry after reduction).

Perform minimization procedure to find the nonstoichiometry after reduction **(d_f)** knowing the relationship in between p_{O_2}, T, and δ given by (1.52):

$$\ln p_{O_2}(\delta,T)^{1/2} = -\left(\frac{1}{T}\right)\frac{\Delta h_o(\delta)}{R} + \frac{\Delta s_o(\delta)}{R} \qquad (1.52)$$

Define function *objective_red* depending only on delta **(d)** similar to Example Question 6. However, the minimization procedure will repeat using a *for loop* for every temperature of reduction **(T_H)**. Then, the values of delta **(d)** will be stored in the array **(d_f)** for later use.

```
In [20]:  #Define variables and fixed parameters
          T_H = np.array([2073, 1973, 1873, 1773, 1673, 1573])  #(K)
          p_O2 = 1e-5  #(atm)
          d_f = np.array([])
```

```
In [21]:  for i in range(0, T_H.size):
              def objective_red(d):
                  return np.abs(np.log(p_O2**0.5)+(poly(d,*coeff1)/(T_H[i]*R))-(po
          ly(d,*coeff2)/(1000*R)))

              initial_guess_red = 0.01

              #Minimize function objective_red
              sol_red = minimize(objective_red, initial_guess_red, method='SLSQP',
          tol=1e-10, options={'disp': False}, bounds=[(0,0.2)])
              d_f = np.append(d_f, sol_red.x[0])
```

Perform minimization procedure to find nonstoichiometry after oxidation **(d_i)** similar to Example Question 6. Define function *objective_ox* depending only on delta **(d)**. The minimization procedure will repeat using a *for loop* for different temperatures of oxidation in the range $800\ \mathrm{K} < T_{\mathrm{L}} < 1200\ \mathrm{K}$. Then the values of delta **(d)** will be stored in the **(H_2)** array, remembering that $H_2 = \delta_{\mathrm{f}} - \delta_{\mathrm{i}}$.

```
In [22]:  #Define variables and fixed parameters
          n_H2O = d_f  #(mol)
          T_L = np.arange(800,1200,10)  #(K)
```

```
In [23]:  for ii in range(0, d_f.size-1):
              H_2 = np.array([])
              for i in range(0, T_L.size):
                  def objective_ox(d):
                      return np.abs(poly(d,*coeff1)-poly(d,*coeff2)*T_L[i]/1000+(R
          *T_L[i]*np.log((n_H2O[ii]-(d_f[ii]-d))/((d_f[ii]-d)*10**(linear((1/T_L[i
          ]),*coeff3))))))

                  initial_guess_ox = 0.01

                  #Minimize function objective_ox
                  sol_ox = minimize(objective_ox, initial_guess_ox, method='SLSQP'
          , tol=1e-10, options={'disp': False}, bounds=[(0,0.2)])
```

```
                H_2 = np.append(H_2, d_f[ii]-sol_ox.x[0])

            #For every T_H plot H_2 productivity as a function of T_L
            plt.plot(T_L, H_2, 'r')
            plt.plot(T_L, np.repeat(d_f[ii], 40), 'b--', linewidth=1)
            plt.xlabel('Oxidation Tempertature, '+' $T_L (K)$')
            plt.ylim(0, 0.2)
            plt.ylabel('$H_2$'+' Productivity')

        #Plot image with labels and text to reproduce original image as accurate
        ly as possible
        plt.text(810, 0.182, '$T_H=2073$ K')
        plt.text(810, 0.16, '$1973$ K')
        plt.text(810, 0.105, '$1873$ K')
        plt.text(810, 0.065, '$1773$ K')
        plt.text(810, 0.042, '$1673$ K')
        plt.text(810, 0.024, '$1573$ K')
        plt.plot(T_L, np.repeat(d_f[5], 40), 'b--', linewidth=1)
        plt.title('$H_2$ Productivity versus Oxidation Temperature')
        plt.show()
```

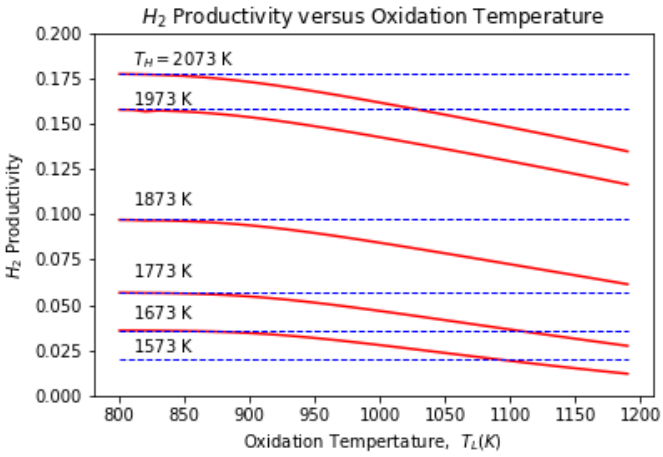

Efficiency of Redox Cycles

The solar to fuel conversion efficiency ($\eta_{\text{solar-to-fuel}}$) of thermochemical redox cycles is strongly tied to the temperature difference between reduction (T_{red}) and oxidation (T_{ox}) steps and the oxidation conversion at T_{ox} ($n_{\text{H2}}/n_{\text{H2O,i}}$). The former is related to the fact that the metal oxide must be heated each cycle from T_{ox} to T_{red} and the latter is related to the sensible energy required to heat the H_2O or CO_2 from ambient conditions to T_{ox}. A schematic of the cycle indicating the most pertinent heat transfer and mass flows is shown in Figure 16. Here, the material considered is nonstoichiometric ceria but the analysis may be applied to any two step redox cycle. An energy balance for this system yields.

$$Q_{\text{solar},1} + Q_{\text{solar},2} + \left(h_{\text{H2O}}\big|_{T_{\text{OX}}} - h_{\text{H2O}}\big|_{T\text{amb}}\right) n_{\text{H2O,i}} = Q_{\text{re-rad, sensible}} + Q_{\text{re-rad, red}} + Q_{\text{rejection}} + Q_{\text{oxidation}}$$
$$+ \left(h_{\text{O2}}\big|_{T_{\text{RED}}} - h_{\text{O2}}\big|_{T\text{amb}}\right) n_{\text{O2}} + \left(h_{\text{H2O}}\big|_{T_{\text{OX}}} - h_{\text{H2O}}\big|_{T\text{amb}}\right) n_{\text{H2O}} + \left(h_{\text{H2}}\big|_{T_{\text{OX}}} - h_{\text{H2}}\big|_{T\text{amb}}\right) n_{\text{H2}} + \text{HHV}_{\text{H2}} n_{\text{H2}} \quad (1.60)$$

$Q_{solar,1}$ is the solar energy required to heat the oxide from T_{ox} to T_{red}, $Q_{solar,2}$ is the solar energy needed to reduce the oxide, $Q_{re\text{-}rad,\ sensible}$ and $Q_{re\text{-}rad,\ red}$ are the radiative losses during sensible heating and reduction, $Q_{rejection}$ is the energy rejected from the system to cool the particles from T_{red} to T_{ox}, $Q_{oxidation}$ is the energy rejected from the system during exothermic oxidation, h_i is the specific enthalpy of species i at the specified temperature and n_i is the number of moles of species i. HHV_{H2} is the higher heating value of H_2 and included in the energy balance assuming that the H_2 produced may be combusted to produce heat. $Q_{solar,1}$ is related to the sensible energy stored in the oxide, $Q_{sensible}$, through the following relationships.

$$Q_{sensible} = Q_{solar,1} - Q_{rerad,sensible} \quad (1.61)$$

$$Q_{sensible} = n_{CeO2} \int_{T_{OX}}^{T_{RED}} c_p dT \quad (1.62)$$

For ceria, specific heat data is available from several resources as a function of temperature and nonstoichiometry and extrapolation is applied for high temperatures where data is not available [70]. $Q_{solar,2}$ is related to the enthalpy change of the oxide during reduction, Q_{red}, which is related to the partial molar enthalpy of ceria and should be integrated over the change in nonstoichiometry, as shown below.

$$Q_{red} = Q_{solar,2} - Q_{rerad,red} \quad (1.63)$$

$$Q_{red} = n_{CeO_2} \int_{\delta_f}^{\delta_i} \Delta h_o d\delta \quad (1.64)$$

The addition of solar energy to the system via an aperture means that the radiative losses $Q_{re\text{-}rad,sensible}$ and $Q_{re\text{-}rad,red}$ must be accounted for. These terms may be calculated assuming a blackbody cavity emitting radiation to the surroundings that are at ambient temperature. Because these terms do not necessarily occur at constant temperature, the losses should be integrated over the temperatures and times during which the heat transfer occurs. However, to simplify things it is usually assumed that the radiative losses all occur at the highest temperature, T_{red}, in which case they become equal to,

$$\left(Q_{re\text{-}rad,\ sensible} + Q_{re\text{-}rad,\ red}\right) = Q_{rad} = \left(1-\eta_{abs}\right)\left(Q_{solar,1} + Q_{solar,2}\right) \quad (1.65)$$

where Q_{rad} is the total radiative heat transfer losses and η_{abs} was defined prior in equation (1.4) . Therefore, knowing the equilibrium yield of H_2 which is a function of the initial reduction extent (which is a function of T_{red} and p_{O2}), $n_{H2O,0}$ and T_{red}, the solar-to-fuel conversion efficiency ($\eta_{solar\text{-}to\text{-}fuel}$) can be calculated as a function of each of these parameters according to the standard efficiency definition below.

$$\eta_{solar\text{-}to\text{-}fuel} = \frac{W_{out}}{Q_{in}} = \frac{n_{H2} HHV_{H2}}{Q_{solar,1} + Q_{solar,2} + \left(h_{H2O}\big|_{T_{OX}} - h_{H2O}\big|_{Tamb}\right) n_{H2O,i}} \quad (1.66)$$

It should be noted that energy inputs can be decreased with heat exchangers that take advantage of the hot gases exiting the system and heat rejection from solids that are recirculated within the system boundary, for

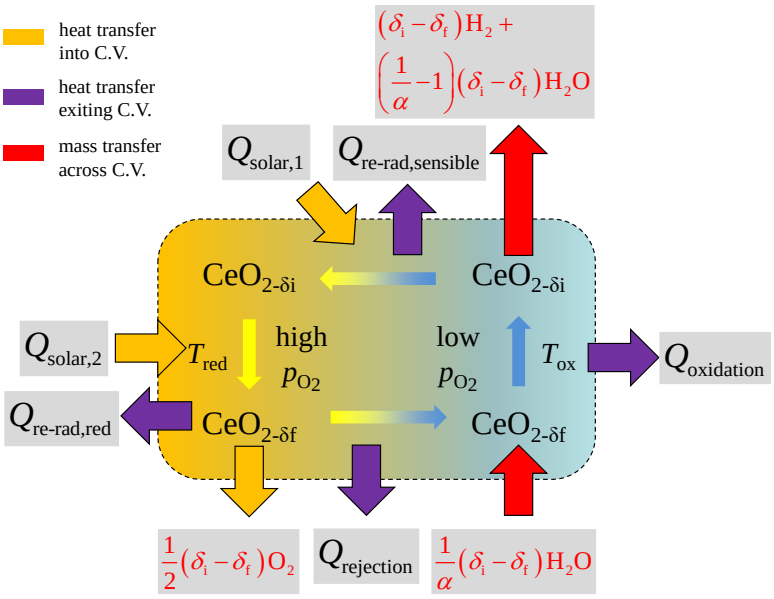

Figure 16. Heat and mass flows that accompany a ceria based thermochemical cycle; the analysis is conceptually similar for any two step thermochemical cycle. The major energy components required to drive the cycle is a result of energy required to heat the oxide ($Q_{sensible}$), reduce it (Q_{red}), offset the radiative losses ($Q_{re\text{-}rad,sensible}$ and $Q_{re\text{-}rad,red}$) and heat the steam (or CO_2).

example when cooling or during oxidation. For example, solid-solid heat exchangers that recuperate heat as particles are cooling from T_{red} to T_{ox} as Sandia's CR5 and circulating particle reactor operate[56, 71], or gas-gas heat exchangers that take advantage of the hot gases exiting the system like in the University of Minnesota's solar reactor[72]. There are numerous research papers that deal with this topic and investigate the impact that heat exchange, operation temperatures and pressures have on the overall theoretical efficiency[45-48, 73-75]. In general, depending on the operating conditions and degree of heat recuperation, $\eta_{solar\text{-}to\text{-}fuel}$ can vary between only a few percent (e.g. during isothermal operation of reduction and oxidation steps and no heat recuperation) to 50% when using ceria. It should be noted that these values do not account for any spillage of solar radiation and typically heat losses except for radiation. Further, the energy required to obtain the oxygen partial pressures in the range of 10^{-3} to 10^{-5} atm during the reduction step are not included here but should be for a more thorough analysis; depending on the pressures assumed these may not be insignificant values. For example, it is typical to use and inert sweep gas such as Ar, which requires energy to produce, or vacuum pumping which requires mechanical work. The highest reported experimental efficiency is 5.25 % as reported by Marxer *et al.* in 2017 using ceria and vacuum pumping during reduction[76]. They note that vacuum pumping has the added benefit of limiting the heat transfer through the sides of their reactor. Seasonal variations regarding DNI and its impact on total fuel yields should also be considered when evaluating the overall economic cost of such a system. The economics are strongly tied to the solar-to-fuel conversion efficiency and have been discussed in several works[46, 77, 78]. This is because the size of the concentrating infrastructure is the largest cost contributor and this size directly scales with efficiency. For example, a thermochemical cycle that is twice as efficient as another will require half the concentrating area to produce the same amount of fuel (assuming equal concentration ratios and spillage) and thus the concentrating equipment cost will be roughly cut in half.

Chueh *et al.* discuss how the efficiency of a ceria based thermochemical cycle varies as a function of T_{red} and T_{ox} assuming that only a limited amount of H_2O is introduced into the system to drive oxidation; namely $n_{H2O,i} = \delta_f$. A summary of their results is shown below in Figure 17. As seen, the efficiency largely scales with the amount of H_2 produced and the temperature swing required to produce it. For example, focusing on subplot a of Figure 17, the most H_2 is produced where ceria has been most reduced (i.e. at the highest reduction temperature of 2073 K). Looking at the subsequent subplot in Figure 17b, it is clear that efficiency largely scales with these yields, but there are optimal oxidation temperatures where the efficiency is maximized. This is because for the highest oxidation temperatures, H_2 yields begin to decrease, and at the

lowest temperatures, the temperature swing and thus heating demands of the solid increase. This can be seen in Figure 17d where all of the enthalpy terms per mol of H_2 are tabulated versus reduction temperature. As seen, for the lowest reduction temperatures, the largest contributor is the enthalpy required to heat ceria. As the reduction temperature increases along with increasing yields of H_2, this contribution decreases, resulting in overall higher efficiencies.

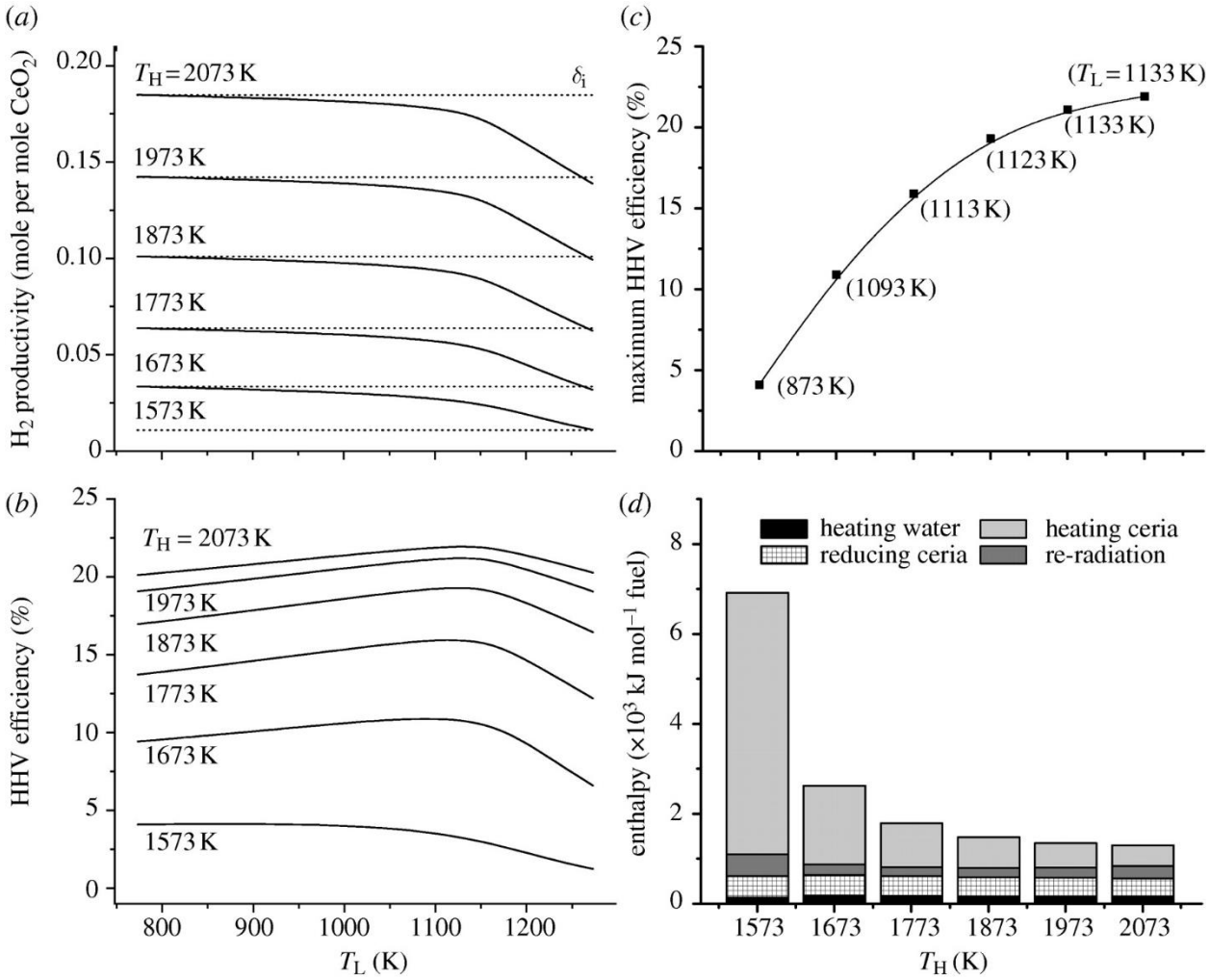

Figure 17. From Chueh et al. a) H_2 productivity versus oxidation temperature (here shown as T_L), for fixed reduction temperatures, T_H. As seen for low T_L, ceria is almost fully oxidized and $n_{H2} = \delta_i$ (here δ_i is the nonstoichiometry after reduction, or δ_i as we have referred to it). b) $\eta_{solar\text{-}to\text{-}fuel}$ versus T_H and T_L. c) Maximum efficiency versus T_H. d) Energy flows related to heating H_2O, heating ceria, reduction of ceria and re-radiation. For all calculations, $p_{O2}=10^{-5}$ atm during reduction and for oxidation $n_{H2O,i} = \delta_i$.

Experimental Demonstration of the Ceria Based Cycle

There have been a number of prototype solar reactors proposed and developed for a number of metal oxide redox pairs other than ceria [56, 79-85]. In recent years however, the overwhelming majority of reactors have been focused on ceria based redox cycles because of its aforementioned favorable properties. The reactors vary from particle based systems[71, 86] that propose circulating particles through separate reduction and

oxidation reactors, to batch type systems[67, 68, 72, 76, 87] where ceria is stationary and the operating conditions within the reactor are varied with time to drive either reduction or oxidation.

Because of the simplicity of batch type systems, these have been especially attractive and to date have set the record for solar thermochemical splitting efficiencies, starting in 2010 when Chueh *et al*. demonstrated the dissociation of CO_2 and H_2O in a cavity type receiver using porous ceria bricks housed inside. Here they demonstrated efficiencies of less than 1%. Importantly, they recognized that the low efficiencies were resultant of the fact that their reaction rates during reduction where solar energy is supplied were limited by heat transfer.[67] Following this, Furler *et al*. aimed to improve heat transfer rates by producing reticulated porous ceramic (RPC) ceria parts that act as more effective volumetric absorbers of radiation because of their large pore sizes; they demonstrated CO_2 splitting efficiencies of 1.73%[68]. While this represented a dramatic improvement because of improved heat transfer, the authors recognized that oxidation reaction rates were kinetically limited and much slower compared to the prior Chueh *et al*. work as a result of the large length scales (and specific surface area) inherent to RPC's. Therefore, RPC's by the same authors were then developed with dual scale pore sizes; large pores for efficient and volumetric absorption of solar radiation where heat transfer is limiting and small pores to increase the specific surface area and hence oxidation rates, where kinetics are rate limiting[87].

Recently Marxer *et al*. demonstrated CO_2 splitting efficiencies with this duel scale RPC of 5.25%[76]. Also impressively, they demonstrated 500 consecutive redox cycles and 100% selectivity of CO_2 to CO with 83% molar conversion. A schematic and photograph of the reactor that was utilized, along with the RPC is shown in Figure 18. As seen, the RPC is contained within the cavity receiver and is enclosed with a quartz window to separate it from the ambient environment. The reactor is operated by first subjecting the ceria RPC to concentrated solar radiation at either ambient pressure with a sweep gas or reduced pressure (10 mbar) with vacuum pumping, resulting in oxygen evolution. Following this, the temperature is cooled by removing the concentrated solar radiation (in this case by turning off the solar simulator that was utilized

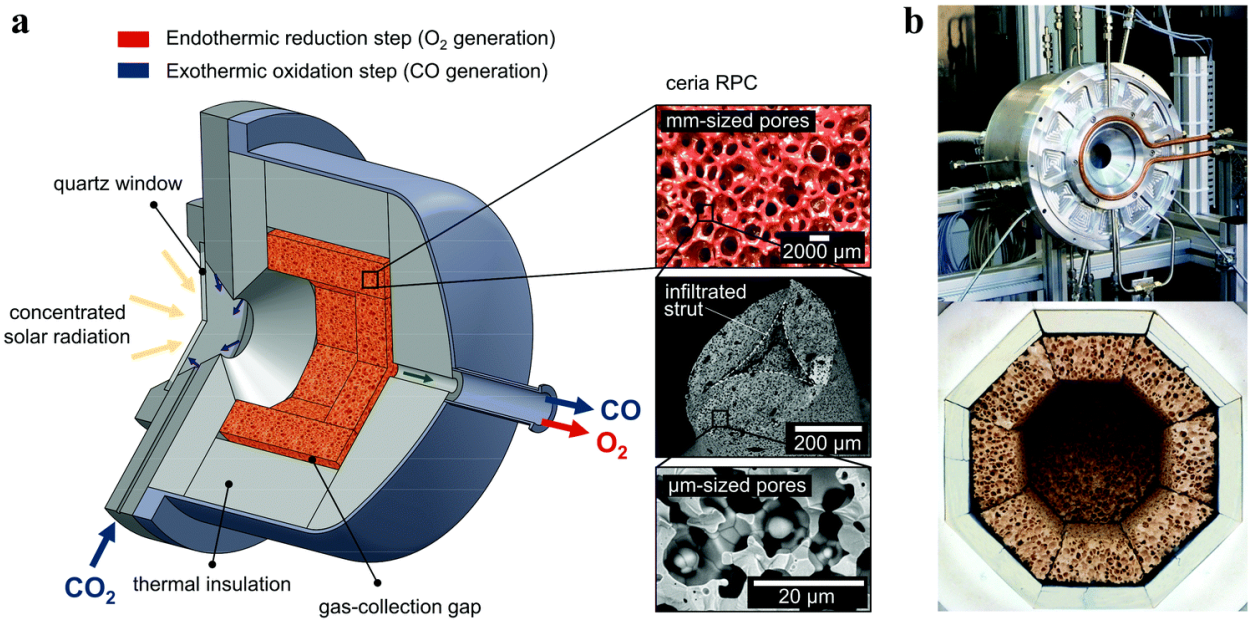

Figure 18. Schematic of ceria based cavity reactor developed by Marxer *et al*. This system utilizes a dual scale RPC that serves as a good solar absorber and enhances heat transfer during reduction and has high specific surface area to enhance oxidation reaction rates.

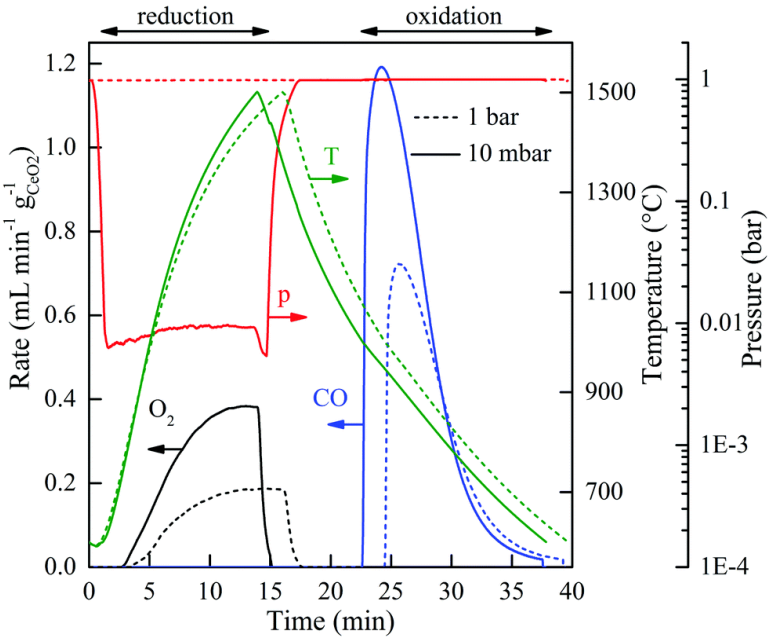

Figure 19. Experimental results during operation of Marxer et al.'s solar reactor. On the left is reduction that is initiated by introducing concentrated radiation into the cavity. As a result the temperature increases and oxygen production rates increase. This is followed by oxidation of ceria with CO_2 to produce CO that is initiated by decreasing the solar flux incident into the reactor, causing the temperature to decrease.

but there are practical ways to do this on a real solar furnace) and introducing CO_2 into the system to produce CO.

Experimental results of the aforementioned reactor are shown below in Figure 19. The left hand side of the figure shows the reduction reaction and plots the temperature shown in green and the corresponding oxygen evolution in black (solid lines correspond to vacuum operation and dashed to ambient pressure). As seen, when the similar power is increased at time = 0 min, the temperature begins to increase to a peak of 1500 °C, alongside the oxygen which scales with temperature. Here, the reaction is not driven to equilibrium, as indicated by the rapid decrease in oxygen production rates because of a decrease in power input. This is related to the fact that optimal efficiency does not usually occur if reaction extents are driven to equilibrium because of diminishing yields with time, even while the power input to maintain the temperature remains roughly constant. Once the temperature decreases to about 1100 °C, CO_2 is injected into the reactor and a large increase in CO production is seen, followed by a slower decline. Once completed, the cycle is re-initiated by stopping the delivery of CO_2 and increasing the power input again. From these results, it can be seen that the reduction and subsequent oxidation yields are greater during vacuum operation, and as a result efficiencies were greatest when operating the cycle below ambient pressure. This was primarily a result of the fact that the reduction rates were enhanced with vacuum operation and heat losses were decreased across the insulation to the outside of the cavity because of decreased convective losses. This record thermochemical efficiency of 5.25% is competitive with benchmark's set by PV combined with CO_2 electrolysis[88].

Emerging Redox Materials

In recent years, there have been a host of new oxides that have shown promise when it comes to improvement over ceria. The major driving force for these materials comes from the fact that in order for ceria to maximize its efficiency, temperatures on the order of 1500 °C and higher should be used. This is related to the fact that the reduction extent at lower temperatures is relatively small at the pressures typically used, which puts an upper limit on the H_2 yields and thus efficiency. When operating at temperatures of 1500 °C or higher, the robustness of ceria regarding sintering, its reactivity with other reactor components, sublimation and the stability of reactor components all come into play. When operating at an average temperature of 1500 °C, locations where the radiation is incident can be even hundreds of degrees hotter and suffer most severely. Further, the demands on concentrating optics to achieve the concentration ratios necessary with limited losses due to spillage have not been developed, at least for heliostat driven tower based systems: these usually operate at temperatures lower than 1000 °C. In general, there have been a host

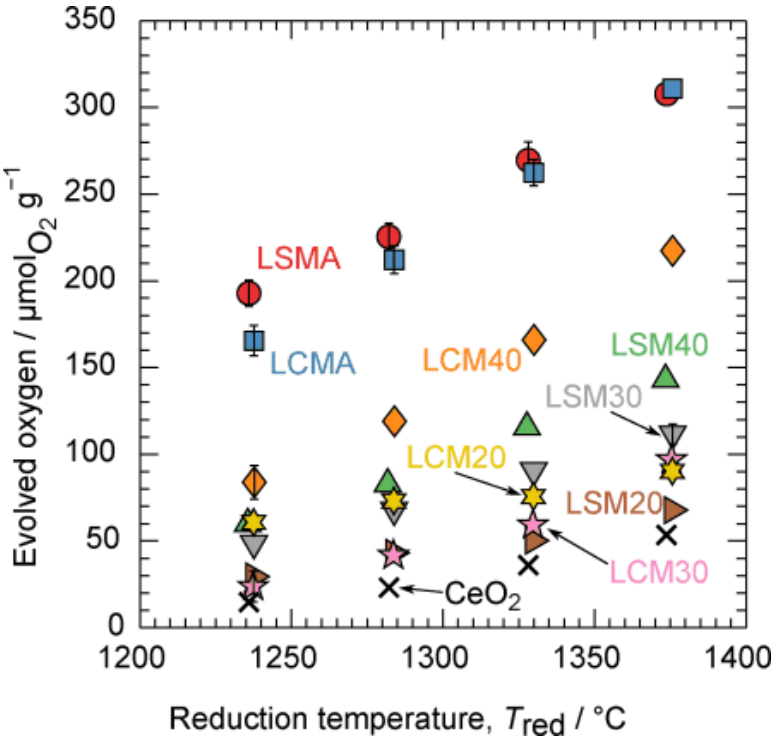

Figure 20. Measured amounts of evolved oxygen from thermogravimetric analysis. From Cooper et al. The letters in the acronym stand for the cations (e.g. L=La) and the number represents the number of moles (times 100) of second cation doped on the A-site.

of materials proposed, but initially they were al based on various forms of doped ceria using Zr^{4+}, Hf^{4+} and others[89, 90]. In general the 4+ dopants were all shown to reduce at more moderate temperatures than ceria and in general increase reduction extent with increasing degree of doping. For lower valence dopants however, this effect was suppressed[91]. In 2013, two classes of perovskites were proposed based on La-Sr-Mn[92] and La-Sr-Mn-Al[93] systems. The perovskites, of the form $ABO_{3-\delta}$, were also shown to be more easily reduced than ceria and McDaniel *et al*. demonstrated fuel productivity on the order of 5 times ceria (albeit for low reduction temperatures of 1350 °C where ceria is not readily reduced)[93]. From there, a host of related perovskite compositions have been proposed, including La-Ca-Mn[69, 94], La-Ca-Mn-Al[69, 94], Y-Sr-Mn[95], and La-Sr-Cr-Co[96], all of which have shown the ability to reduce more readily than ceria. More recently papers have been published promoting materials based on $BaCe_{0.25}Mn_{0.75}O_{3-\delta}$ and poly cation oxides of the family $(FeMgCoNi)O_x$ ($x \approx 1.2$). Cooper *et al*. nicely compare the oxygen yields of a select number of $La_{1-x}(Sr,Ca)_xMn_{1-y}Al_yO_3$ perovskites with ceria, as shown in Figure 20[69]. The letters in the acronym stand for the cations (e.g. L=La) and the number represents the number of moles (times 100) of second cation doped on the A-site. In general, for both Ca^{2+} and Sr^{2+} doped LSM and LCM perovskites, evolved oxygen increases in increasing A site doping concentration (except for LCM20 and LCM30) and for 20, 30 and 40 mol-% A-site dopant concentrations they all reduce more readily than pure ceria. When Al^{3+} is doped on the B-site (i.e. LSMA and LCMA where A-site Sr^{2+} and Ca^{2+} concentrations are 40 mol-% and B-site Al^{3+} concentrations are 40 mol-%), reduction extents are even greater. Overwhelmingly, there is a strong correlation between the reduction enthalpy and the oxygen evolution at a given reduction temperature; namely, as the reduction enthalpy decreases, so too does the reduction temperature. This makes sense given that the driving force for reduction, or Gibbs free energy change of the reaction, is directly related. These trends are discussed in detail in a recent review paper by Carrillo *et al*.[64].

While all of these materials can more easily reduce than ceria, reduction ability is only half of the story. The materials also must have an affinity for oxidation with H_2O, which is also tied to the reduction enthalpy. The lower it is, the closer it becomes to the enthalpy required to split water, and eventually at the point where its magnitude is lower, the cycle is no longer tenable. Such a scenario can be imagined with a figure similar to Figure 8 but with a lower enthalpy, in which case the red curve indicating oxidation favorability would always be greater than zero. The implications of this on fuel yields can be observed in Figure 21 below from Cooper *et al*. In this figure that shows predicted equilibrium yields from thermodynamic

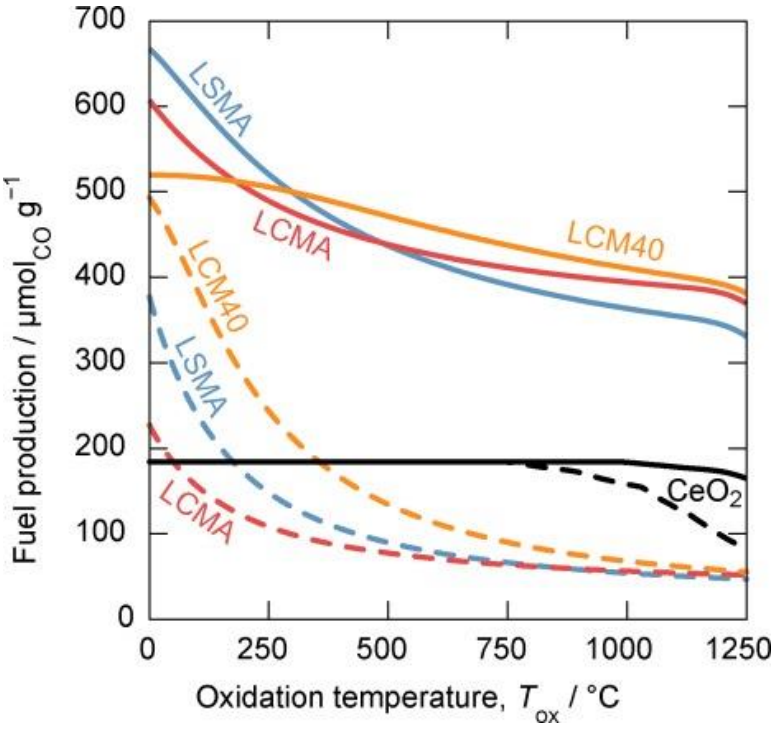

Figure 21. From Cooper *et al*. Predicted equilibrium yields from thermodynamic calculations, all samples have first been subjected to reduction conditions at 1400 °C and p_{O2} = 10^{-5} atm. The reduction extents are δ_f = 0.15, 0.13, 0.11, and 0.03 for LSMA, LCMA, LCM40, and CeO_2, respectively. Following this, reduced samples are then oxidized with either 1 mol CO_2 per mol oxide (dashed lines) or 100 mol CO_2 per mole oxide (solid lines).

calculations, all samples have first been subjected to reduction conditions at 1400 °C and p_{O2} = 10^{-5} atm. The reduction extents are δ_f = 0.15, 0.13, 0.11, and 0.03 for LSMA, LCMA, LCM40, and CeO_2, respectively. Following this, reduced samples are then oxidized with either 1 mol CO_2 per mol oxide (dashed lines) or 100 mol CO_2 per mole oxide (solid lines). Although all of the perovskites reduce substantially more than ceria, the oxidation yields when oxidant amounts are low are lower than ceria under most conditions (high temperature). For example, consider the dashed LCM40 sample that is initially reduced to δ_f = 0.11 versus ceria that is reduced to δ_f = 0.03. The fuel yields are lower than ceria until about 400 °C where oxidation becomes more favorable and the oxidation conversions increase; at this temperature and lower, the kinetics would likely be to slow for the cycle to be tenable. When the oxidant yields are increased by a factor of 100, the fuel yields for all perovskites are higher than ceria, but at the expense of excess heating requirements which will hinder the efficiency. These results highlight the importance of considering oxidation favorability as well as reduction extent when evaluating candidate redox materials. Ultimately, only a thermodynamic analysis that couples reaction equilibrium of both reduction and oxidation steps with required heat and mass flows can predict the potential suitability of materials to be used in thermochemical redox cycles.

References

[1] J. Duffie, W. Beckman, Solar Engineering of Thermal Processes, **2013**.
[2] A. T. Mecherikunnel, J. C. Richmond in Spectral Distribution of Solar Radiation, Vol. (Ed.^Eds.: Editor), NASA, City, **1980**.
[3] S. Chu, Y. Cui, N. Liu *Nature Materials*. **2016**, *16*, 16.
[4] NIST-JANAF in NIST-JANAF Thermochemical Tables, Vol. (Ed.^Eds.: Editor), City, **2013**.
[5] J. Larminie, A. Dicks, M. S. McDonald, Fuel cell systems explained, J. Wiley Chichester, UK, **2003**.
[6] C. M. White, R. R. Steeper, A. E. Lutz *International journal of hydrogen energy*. **2006**, *31*, 1292-1305.
[7] N. S. Lewis *Science*. **2016**, *351*.
[8] S. C. Roy, O. K. Varghese, M. Paulose, C. A. Grimes *ACS Nano*. **2010**, *4*, 1259-1278.
[9] **C. Honsberg**, **S. Bowden** in PVEDUCATION.ORG, Vol. (Ed.^Eds.: Editor), City.

[10] R. Van de Krol, M. Grätzel, Photoelectrochemical hydrogen production, Springer, **2012**.
[11] E. Alonso, A. Gallo, C. Pérez-Rábago, E. Fuentealba in Thermodynamic study of CuO/Cu2O and Co3O4/CoO redox pairs for solar energy thermochemical storage, Vol. 1734 (Ed.^Eds.: Editor), AIP Publishing LLC, City, pp.050004.
[12] J. R. Scheffe, A. Steinfeld *Materials Today*. **2014**, *17*, 341-348.
[13] A. Steinfeld, A. Meier *Encyclopedia of energy*. **2004**, *5*, 623-637.
[14] M. Romero, A. Steinfeld *Energy & Environmental Science*. **2012**, *5*, 9234-9245.
[15] A. Steinfeld, R. Palumbo *Encyclopedia of physical science and technology*. **2001**, *15*, 237-256.
[16] R. Winston, J. C. Miñano, P. G. Benitez, Nonimaging optics, Academic Press, **2005**.
[17] J. Chaves, Introduction to nonimaging optics, CRC press, **2017**.
[18] E. A. Fletcher, R. L. Moen *Science*. **1977**, *197*, 1050.
[19] J. M. Smith, H. C. Van Ness, M. M. Abbott *Sat*. **1996**, *18*, 1-3.
[20] N. Piatkowski, C. Wieckert, A. W. Weimer, A. Steinfeld *Energy & Environmental Science*. **2011**, *4*, 73-82.
[21] J. K. Dahl, A. W. Weimer, A. Lewandowski, C. Bingham, F. Bruetsch, A. Steinfeld *Industrial & Engineering Chemistry Research*. **2004**, *43*, 5489-5495.
[22] Q. Liu, H. Jin, H. Hong, J. Sui, J. Ji, J. Dang *International Journal of Energy Research*. **2011**, *35*, 52-60.
[23] D. W. Gregg, R. W. Taylor, J. H. Campbell, J. R. Taylor, A. Cotton *Solar Energy*. **1980**, *25*, 353-364.
[24] A. Z'Graggen, P. Haueter, G. Maag, A. Vidal, M. Romero, A. Steinfeld *International Journal of Hydrogen Energy*. **2007**, *32*, 992-996.
[25] M. Kruesi, Z. R. Jovanovic, A. Haselbacher, A. Steinfeld *AIChE Journal*. **2015**, *61*, 867-879.
[26] T. Melchior, C. Perkins, P. Lichty, A. W. Weimer, A. Steinfeld *Chemical Engineering and Processing: Process Intensification*. **2009**, *48*, 1279-1287.
[27] M. Kruesi, Z. R. Jovanovic, A. Steinfeld *Fuel*. **2014**, *117, Part A*, 680-687.
[28] P. Lichty, C. Perkins, B. Woodruff, C. Bingham, A. Weimer *Journal of Solar Energy Engineering*. **2010**, *132*, 011012-011012-011017.
[29] N. Piatkowski, C. Wieckert, A. Steinfeld *Fuel Processing Technology*. **2009**, *90*, 360-366.
[30] R. Zheng, R. Diver, D. Caldwell, B. Fritz, R. Cameron, P. Humble, W. TeGrotenhuis, R. Dagle, R. Wegeng *Energy Procedia*. **2015**, *69*, 1192-1200.
[31] J. Lede, F. Lapicque, J. Villermaux, B. Cales, A. Ounalli, J. F. Baumard, A. M. Anthony *International Journal of Hydrogen Energy*. **1982**, *7*, 939-950.
[32] A. J. Traynor, R. J. Jensen *Industrial & Engineering Chemistry Research*. **2002**, *41*, 1935-1939.
[33] E. D. Glandt, A. L. Myers *Industrial & Engineering Chemistry Process Design and Development*. **1976**, *15*, 100-108.
[34] J. E. Funk, R. M. Reinstrom *Industrial & Engineering Chemistry Process Design and Development*. **1966**, *5*, 336-342.
[35] E. Bilgen, C. Bilgen *International journal of hydrogen energy*. **1982**, *7*, 637-644.
[36] T. Nakamura *Solar Energy*. **1977**, *19*, 467-475.
[37] L. Darken, R. W. Gurry *Journal of the American Chemical Society*. **1945**, *67*, 1398-1412.
[38] I. Bransky, A. Z. Hed *Journal of the American Ceramic Society*. **1968**, *51*, 231-231.
[39] O. N. Salmon *The Journal of Physical Chemistry*. **1961**, *65*, 550-556.
[40] J. Nowotny, M. Rekas *Journal of the American Ceramic Society*. **1989**, *72*, 1221-1228.
[41] A. D. Pelton, H. Schmalzried, J. Sticher *Berichte der Bunsengesellschaft für physikalische Chemie*. **1979**, *83*, 241-252.
[42] M. D. Allendorf, R. B. Diver, N. P. Siegel, J. E. Miller *Energy & Fuels*. **2008**, *22*, 4115-4124.
[43] N. Jacobson *J. Chem. Educ*. **2001**, *78*, 814.
[44] W. C. Chueh, S. M. Haile *Philosophical Transactions of the Royal Society of London A: Mathematical, Physical and Engineering Sciences*. **2010**, *368*, 3269-3294.
[45] J. Lapp, J. H. Davidson, W. Lipiński *Energy*. **2012**, *37*, 591-600.

[46] N. P. Siegel, J. E. Miller, I. Ermanoski, R. B. Diver, E. B. Stechel *Industrial & Engineering Chemistry Research*. **2013**, *52*, 3276-3286.
[47] I. Ermanoski, J. E. Miller, M. D. Allendorf *Physical Chemistry Chemical Physics*. **2014**, *16*, 8418-8427.
[48] M. Lin, S. Haussener *Energy*. **2015**, *88*, 667-679.
[49] A. Steinfeld, S. Sanders, R. Palumbo *Solar Energy*. **1999**, *65*, 43-53.
[50] T. Kodama, Y. Nakamuro, T. Mizuno *Journal of solar energy engineering*. **2006**, *128*, 3-7.
[51] P. Charvin, S. Abanades, G. Flamant, F. Lemort *Energy*. **2007**, *32*, 1124-1133.
[52] T. Kodama, N. Gokon, R. Yamamoto *Solar Energy*. **2008**, *82*, 73-79.
[53] J. R. Scheffe, A. H. McDaniel, M. D. Allendorf, A. W. Weimer *Energy & Environmental Science*. **2013**, *6*, 963-973.
[54] J. E. Miller, M. D. Allendorf, R. B. Diver, L. R. Evans, N. P. Siegel, J. N. Stuecker *Journal of Materials Science*. **2008**, *43*, 4714-4728.
[55] E. N. Coker, A. Ambrosini, M. A. Rodriguez, J. E. Miller *Journal of Materials Chemistry*. **2011**, *21*, 10767-10776.
[56] R. B. Diver, J. E. Miller, N. P. Siegel, T. A. Moss. **2010**, 97-104.
[57] P. G. Loutzenhiser, A. Meier, A. Steinfeld *Materials*. **2010**, *3*.
[58] A. Stamatiou, P. G. Loutzenhiser, A. Steinfeld *Chemistry of Materials*. **2010**, *22*, 851-859.
[59] S. Abanades, P. Charvin, F. Lemont, G. Flamant *International Journal of Hydrogen Energy*. **2008**, *33*, 6021-6030.
[60] C. Perkins, A. W. Weimer *International Journal of Hydrogen Energy*. **2004**, *29*, 1587-1599.
[61] A. Steinfeld *Solar Energy*. **2005**, *78*, 603-615.
[62] T. Kodama, N. Gokon *Chemical Reviews*. **2007**, *107*, 4048-4077.
[63] J. E. Miller, A. H. McDaniel, M. D. Allendorf *Advanced Energy Materials*. **2014**, *4*, 1300469-n/a.
[64] R. J. Carrillo, J. R. Scheffe *Solar Energy*. **2017**.
[65] W. C. Chueh, S. M. Haile *ChemSusChem*. **2009**, *2*, 735-739.
[66] R. J. Panlener, R. N. Blumenthal, J. E. Garnier *Journal of Physics and Chemistry of Solids*. **1975**, *36*, 1213-1222.
[67] W. C. Chueh, C. Falter, M. Abbott, D. Scipio, P. Furler, S. M. Haile, A. Steinfeld *Science*. **2010**, *330*, 1797-1801.
[68] P. Furler, J. Scheffe, M. Gorbar, L. Moes, U. Vogt, A. Steinfeld *Energy & Fuels*. **2012**, *26*, 7051-7059.
[69] T. Cooper, J. R. Scheffe, M. E. Galvez, R. Jacot, G. Patzke, A. Steinfeld *Energy Technology*. **2015**, *3*, 1130-1142.
[70] I. Riess, M. Ricken, J. No¨lting *Journal of Solid State Chemistry*. **1985**, *57*, 314-322.
[71] I. Ermanoski, J. Grobbel, A. Singh, J. Lapp, S. Brendelberger, M. Roeb, C. Sattler, J. Whaley, A. McDaniel, N. P. Siegel in Design and construction of a cascading pressure reactor prototype for solar-thermochemical hydrogen production, Vol. 1734 (Ed.^Eds.: Editor), AIP Publishing, City, pp.120001.
[72] B. J. Hathaway, R. Bala Chandran, A. C. Gladen, T. R. Chase, J. H. Davidson *Energy & Fuels*. **2016**, *30*, 6654-6661.
[73] R. Bader, L. J. Venstrom, J. H. Davidson, W. Lipiński *Energy & Fuels*. **2013**, *27*, 5533-5544.
[74] L. J. Venstrom, R. M. De Smith, Y. Hao, S. M. Haile, J. H. Davidson *Energy & Fuels*. **2014**, *28*, 2732-2742.
[75] R. J. Carrillo, J. R. Scheffe *Energy & Fuels*. **2019**, *33*, 12871-12884.
[76] D. Marxer, P. Furler, M. Takacs, A. Steinfeld *Energy & Environmental Science*. **2017**, *10*, 1142-1149.
[77] J. Kim, C. A. Henao, T. A. Johnson, D. E. Dedrick, J. E. Miller, E. B. Stechel, C. T. Maravelias *Energy & Environmental Science*. **2011**, *4*, 3122-3132.
[78] E. B. Stechel, J. E. Miller *Journal of CO2 Utilization*. **2013**, *1*, 28-36.
[79] N. Gokon, S. Takahashi, H. Yamamoto, T. Kodama *International Journal of Hydrogen Energy*. **2008**, *33*, 2189-2199.

[80] H. Kaneko, T. Kodama, N. Gokon, Y. Tamaura, K. Lovegrove, A. Luzzi *Solar Energy*. **2004**, *76*, 317-322.
[81] M. Chambon, S. Abanades, G. Flamant *AIChE Journal*. **2011**, *57*, 2264-2273.
[82] M. Roeb, M. Neises, J.-P. Säck, P. Rietbrock, N. Monnerie, J. Dersch, M. Schmitz, C. Sattler *International journal of hydrogen energy*. **2009**, *34*, 4537-4545.
[83] H. Kaneko, T. Miura, A. Fuse, H. Ishihara, S. Taku, H. Fukuzumi, Y. Naganuma, Y. Tamaura *Energy & Fuels*. **2007**, *21*, 2287-2293.
[84] E. Koepf, W. Villasmil, A. Meier *Applied Energy*. **2016**, *165*, 1004-1023.
[85] J. P. Säck, S. Breuer, P. Cotelli, A. Houaijia, M. Lange, M. Wullenkord, C. Spenke, M. Roeb, C. Sattler *Solar Energy*. **2016**, *135*, 232-241.
[86] M. Welte, R. Barhoumi, A. Zbinden, J. R. Scheffe, A. Steinfeld *Industrial & Engineering Chemistry Research*. **2016**, *55*, 10618-10625.
[87] P. Furler, J. Scheffe, D. Marxer, M. Gorbar, A. Bonk, U. Vogt, A. Steinfeld *Physical Chemistry Chemical Physics*. **2014**, *16*, 10503-10511.
[88] M. Schreier, L. Curvat, F. Giordano, L. Steier, A. Abate, S. M. Zakeeruddin, J. Luo, M. T. Mayer, M. Grätzel. **2015**, *6*, 7326.
[89] J. R. Scheffe, R. Jacot, G. R. Patzke, A. Steinfeld *The Journal of Physical Chemistry C*. **2013**, *117*, 24104-24114.
[90] M. Takacs, J. R. Scheffe, A. Steinfeld *Physical Chemistry Chemical Physics*. **2015**, *17*, 7813-7822.
[91] J. R. Scheffe, A. Steinfeld *Energy & Fuels*. **2012**, *26*, 1928-1936.
[92] J. R. Scheffe, D. Weibel, A. Steinfeld *Energy & Fuels*. **2013**, *27*, 4250-4257.
[93] A. H. McDaniel, E. C. Miller, D. Arifin, A. Ambrosini, E. N. Coker, R. O'Hayre, W. C. Chueh, J. Tong *Energy & Environmental Science*. **2013**, *6*, 2424-2428.
[94] M. Takacs, M. Hoes, M. Caduff, T. Cooper, J. R. Scheffe, A. Steinfeld *Acta Materialia*. **2016**, *103*, 700-710.
[95] M. M. Nair, S. Abanades *ChemistrySelect*. **2016**, *1*, 4449-4457.
[96] A. H. Bork, M. Kubicek, M. Struzik, J. L. M. Rupp *Journal of Materials Chemistry A*. **2015**, *3*, 15546-15557.